Flattening Filter Free Photon Beams for Treatment of Early-Stage Lung Cancer: An Investigation of Peripheral Dose

by

Joanna E. Mader
B.Sc., Mount Allison University, 2010

A Thesis Submitted in Partial Fulfillment of the
Requirements for the Degree of

MASTER OF SCIENCE

in the Department of Physics and Astronomy

Flattening Filter Free Photon Beams for Treatment of Early-Stage Lung Cancer:
An Investigation of Peripheral Dose

by

Joanna E. Mader
B.Sc., Mount Allison University, 2010

Supervisory Committee

Dr. A. Mestrovic, Co-Supervisor
(Department of Physics and Astronomy)
(BC Cancer Agency - Vancouver Island Centre)

Dr. A. Jirasek, Co-Supervisor
(Department of Physics and Astronomy)

Dr. P. Basran, Departmental Member
(Department of Physics and Astronomy)
(BC Cancer Agency - Vancouver Island Centre)

Supervisory Committee

Dr. A. Mestrovic, Co-Supervisor
(Department of Physics and Astronomy)
(BC Cancer Agency - Vancouver Island Centre)

Dr. A. Jirasek, Co-Supervisor
(Department of Physics and Astronomy)

Dr. P. Basran, Departmental Member
(Department of Physics and Astronomy)
(BC Cancer Agency - Vancouver Island Centre)

ABSTRACT

The purpose of this thesis was to evaluate and compare the peripheral dose associated with VMAT lung SABR treatments for 10X, 6X, and 10X-FFF beams. Flattening Filter Free (FFF) radiotherapy photon beams exhibit high dose rates as compared to standard flattened photon beams. The high dose rates available with FFF beams make them ideal for high dose treatments, such as Volumetric Modulated Arc Therapy (VMAT)-delivery lung Stereotactic Ablative Radiotherapy (SABR), where treatment delivery is longer than that of standard treatments. They are also known to show reductions in treatment head scatter, multi-leaf collimator (MLC) transmission and treatment head leakage radiation, compared to flattened beams. The use of FFF beams for VMAT lung SABR has been shown to significantly reduce treatment delivery time, while maintaining plan quality and accuracy. Another potential advantage of the use of FFF beams for VMAT lung SABR is the reduction in peripheral (out-of-field) dose, due mainly to the reduction in head scatter and treatment head leakage.

The peripheral doses delivered by VMAT Lung SABR treatments using 10X-FFF, 10X and 6X were investigated for the Varian TrueBeam medical linear accelerator.

There were three components to this investigation; (1) Ion chamber measurement of peripheral dose for static open, static MLC and dynamic MLC fields, (2) Validation of Monte Carlo, Acuros XB and AAA algorithms for peripheral dose prediction, and (3) Evaluation of peripheral doses for VMAT lung SABR treatments using the validated Monte Carlo model.

Measurements of out-of field doses for static open, static MLC and dynamic MLC fields showed that 10X-FFF delivered peripheral doses in the range of 30% to 50%, 3% to 40% and 5% to 20% lower than the peripheral doses for flattened beams. Dose calculation algorithm validation showed that AAA and Acuros XB significantly under predicted the dose in the peripheral region. Monte Carlo was found to be the most accurate dose calculation algorithm for peripheral dose prediction. The VMAT lung SABR dose distributions were calculated for both static gantry delivery and arc delivery using the validated Monte Carlo model. For static gantry Monte Carlo simulation, 10X-FFF was found to show a reduction in peripheral dose in the range of 7% to 21% and 7% to 17% when compared to 6X and 10X. For arc delivery Monte Carlo simulation, 10X-FFF was found to deliver a statistically significant reduction in mean peripheral dose compared to 6X in four of the six cases, and was not found to deliver a statistically significant reduction in mean peripheral dose compared to 10X in any of the six cases.

For this type of VMAT lung SABR treatment, 10X-FFF offers a reduction in peripheral dose over 6X. In terms of the benefits of using 10X-FFF for this type of treatment, the reduction in peripheral dose is added to the already-established reduction in treatment times.

Contents

List of Tables

List of Figures

ACKNOWLEDGEMENTS

First, I would like to express my sincere thanks to my supervisor, Dr. Tony Mestrovic, for his support, encouragement, and for the countless discussions and brain-storming sessions that have been immeasurably valuable to this work. This thesis has benefited greatly from his guidance and attention to detail.

Thank you to the entire medical physics group, particularly to my committee members, Dr. Andrew Jirasek and Dr. Parminder Basran, for the useful suggestions and unique perspectives on this project. To my fellow medical physics graduate students, you have truly made this experience an enjoyable one. Thank you for the much-needed moral support and trips to Tim's, as well as for the academic collaboration and encouragement. Thanks in particular to Reid Townson, for his patience, assistance, and Monte Carlo expertise.

To my family and friends from Victoria to Halifax, thank you for your unending love and support throughout my entire academic career. Your belief in me keeps me going.

Finally, I would like to thank the University of Victoria and the BC Cancer Agency for providing the funding and equipment that enabled this project.

Chapter 1

Introduction

The aim of this work is to investigate the radiation dose received by normal tissues during the delivery of high-dose Stereotactic Ablative Radiotherapy treatments for lung cancer. In particular, the out-of-field dose associated with treatment using the novel flattening filter free radiation beam is compared to the out-of-field dose associated with treatments using the standard flattened radiation beam. This is accomplished by direct measurement and computer simulation of the doses for various fields in the out-of-field region, as well as calculation and comparison of the out-of-field doses for several anonymized patient plans.

1.1 Introduction to Radiation Therapy

1.1.1 Background

External beam radiation therapy is the utilization of ionizing radiation to control or damage cancer cells. The aim of any radiation therapy treatment is to deliver a high dose of radiation to the tumour, or target volume, while minimizing the dose to surrounding healthy normal tissues. Modern medical linear accelerators (linacs) can deliver high energy radiation with millimetre precision, in combination with state-of-the-art imaging and treatment planning systems.

Ionizing radiation is defined as radiation with sufficient energy to produce ionization in matter by collision, either directly by a charged particle or indirectly through the production of a charged particle [2]. Ionization in living cells causes damage through the ejection of electrons from atoms or molecules within the cell. Chemical changes occur rapidly (on the order of milliseconds) after ionization, breaking chem-

ical bonds and modifying the structure of cellular macromolecules. Of all cellular macromolecules, DNA is the most critical to the cell's viability. The cell is most susceptible to damage to DNA because of the its importance to cellular function and proliferation, limited supply, and large size [3]. If DNA damage cannot be repaired by one of the cell repair pathways, cell death will occur. This mechanism is exploited in radiation therapy to cause the death of malignant cells.

Radiation therapy is one of the most effective modes of cancer treatment, next to surgery, and is often recommended in combination with surgery and/or chemotherapy. Approximately 50% to 60% of patients diagnosed with cancer internationally could benefit from radiation therapy treatment [4]. In British Columbia 33 % of patients diagnosed with cancer in 2007 to 2009 received radiation therapy within two years of diagnosis [5]. In these years, between 21,000 and 22,000 new cancer cases were diagnosed [6]. Typically, more than 7,000 courses of radiation therapy are delivered in British Columbia per year.

Patients undergoing radiation therapy will follow the same progression: pre-treatment imaging, treatment planning, and then radiation treatment delivery. A planning computed tomograph (CT) is acquired with the patient in the treatment setup position, to obtain a 3 or 4D image. This image is then used by the radiation oncology team to construct an individualized treatment plan according to the patient's geometry and location of the target volume. The treatment plan is generally delivered in several sessions, or "fractions." Common fractionation schemes deliver 1.8 Gy to 2 Gy per fraction, up to a total dose of 40 Gy to 70 Gy [3], depending on the tumour type, location and clinical intent. The patient may undergo daily imaging before radiation delivery, while in the treatment setup position, to ensure accuracy and reproducibility of radiation delivery.

The Medical Linear Accelerator

A modern medical linear accelerator (linac) is a compact device consisting of a gantry isocentrically mounted onto the gantry stand, which houses the major linac control unit. The gantry is able to rotate around the patient support assembly (treatment couch), which allows for radiation delivery to the patient from many different angles (see figure 1.1). The treatment room that houses a medical linac is designed to shield surrounding areas from radiation using a combination of radiation absorbing materials and geometric design.

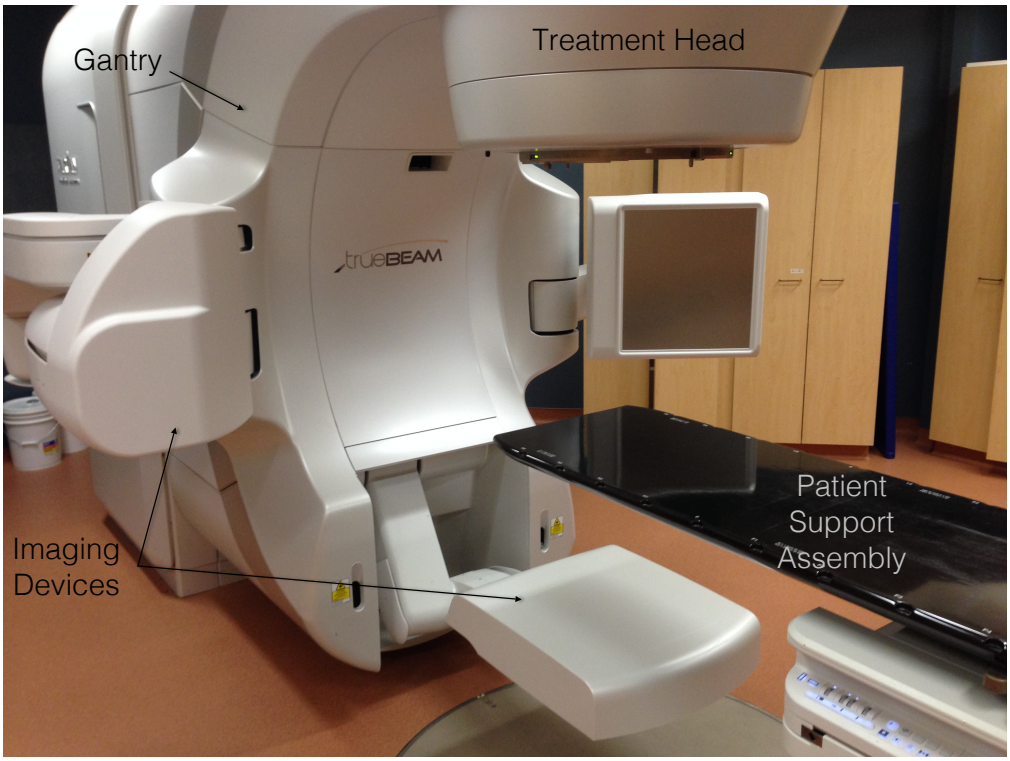

Figure 1.1: Basic components of a medical linear accelerator

Medical linacs use high energy microwaves to accelerate electrons towards a metal target. When the electrons hit the metal target, they produce bremsstrahlung photons which is then shaped into the treatment beam by various collimators and filter components within the treatment head. These different components include the primary and secondary collimators, the multi-leaf collimators (MLC), and the flattening filter, and will be discussed in further detail in chapter 2.

1.1.2 Modern Treatment Techniques

A number of complex treatment techniques have been developed and clinically implemented over the past 15 years that have significantly improved the dose conformality of radiation therapy plans. These techniques employ beam intensity modulation during treatment and utilize multiple gantry angles to achieve highly conformal dose distributions.

Intensity **M**odulated **R**adiation **T**herapy (**IMRT**) is a treatment modality in which "nonuniform fluence is delivered to the patient from any given position of the

treatment beam to optimize the composite dose distribution" [2]. IMRT uses the linac MLC to selectively reduce the radiation fluence through critical structures and increases the fluence for other beam angles [7]. IMRT is made possible by inverse treatment planning, which differs from conventional radiation therapy planning.

Volumetric **M**odulated **A**rc **T**herapy (**VMAT**) is IMRT treatment delivered in an arc, in which the linac gantry rotates around the patient during treatment while delivering beams modulated with the dynamic MLC. Developed in 2008, VMAT treatment planning is accomplished using progressive resolution sampling of gantry and MLC positions, resulting in highly accurate treatment plans, with significantly reduced treatment times [8].

Stereotactic **AB**lative **R**adiotherapy (**SABR**), is a specialized treatment involving the delivery of high doses (more than 2 Gy per fraction) to one or more target volumes within the body, in a small number of fractions (hypofractionation). At the BC Cancer Agency, SABR is used to treat Non-Small Cell Lung Cancer (NSCLC) by delivering 48Gy to a small ($\leq$5 cm diametre) target volume in four fractions, mainly using VMAT delivery [9].

1.2 Flattening Filter Free Beams for lung SABR

Radiation treatment planning has historically necessitated the use of flattening filters to create a uniform photon fluence across the beam. However, today's highly sophisticated radiation therapy treatment planning and delivery systems eliminate this requirement. As a result, the flattening filter traditionally used to produce a uniform intensity photon beams could be removed from the beam line, creating a flattening filter free (FFF) photon beam. FFF beams, which are discussed in detail in chapter 2, have characteristics such as a higher dose rate, lower mean photon energy, and lower out-out-field dose, when compared to standard flattened beams [10, 11].

The removal of the flattening filter for radiotherapy beams was proposed as early as the 1990's, for specialized treatments requiring high dose rates [12]. More recently, with the advent of intensity-modulated body stereotactic treatments, the interest in the use of FFF beams has increased [13] in order to shorten treatment times. The Varian TrueBeam (Varian Medical Systems, Palo Alto, CA) is one of the first commercially available standard medical linacs that offers clinical FFF beam modes.

Radiation therapy can be described as a "double-edged sword," whereby the same process that is used to kill malignant cells can have a significant negative impact on the

surrounding healthy tissues. While every effort is made to minimize the dose received by these tissues, some deposition of radiation dose will be inevitable. One side effect of dose to normal tissues is the induction of secondary cancers as a result of DNA damage. Secondary cancers manifest years after the original treatment, and have been observed in tissues far from the treatment field [14]. For this reason, the out-of-field (peripheral) dose associated with a given treatment should be considered. There is a large body of literature that attempts to quantify and describe the peripheral dose for various treatments, and the risks of secondary cancers associated with them [15]. Highly modulated treatments such as IMRT and VMAT are known to deliver higher peripheral doses than conventional, non-modulated treatments, however they provide benefits such as very conformal dose distributions [16].

The use of FFF beams for VMAT lung SABR has been proposed for several reasons, including the high dose rate offered by FFF beams. Several advantages of using FFF beams for VMAT lung SABR have already been established. Feasibility studies have shown that VMAT and SABR treatments using FFF beams show clinically equivalent dosimetric quality and accuracy to standard beams [17, 18, 19, 20]. Additionally, treatment times have been shown to be significantly reduced when using high-dose rate FFF beams [10, 17]. Lung SABR treatments tend to be longer than standard radiation therapy treatments because they deliver a high dose per fraction. Long treatment times increase the incidence of intra-fractional patient motion and make treatment deliveries less comfortable for patients [17]. As a result, the reduction in treatment time is the most important advantage offered by FFF beams for this type of treatment.

Another potential advantage of using FFF beams for VMAT lung SABR is a reduction in peripheral dose. A reduction in out-of-field dose has been shown for FFF beams in several cases [11, 21]. However, no systematic study exists of the peripheral dose associated with VMAT lung SABR treatments on the Varian TrueBeam (Varian Medical Systems, Palo Alto, CA) linac for FFF and standard flattened beams.

1.3 Thesis Scope

This thesis investigates the peripheral doses associated with VMAT lung SABR treatments on the Varian TrueBeam (Varian Medical Systems, Palo Alto, CA). Measurements of peripheral dose are performed for simple and complex plans using both FFF and flattened beams. Several dose calculation algorithms are assessed for dose

calculation in the peripheral region, through comparison with measurements. The validated dose calculation algorithm is then used to compare the peripheral dose for FFF and flattened beams for several sample patient cases.

Chapter 2 will cover the background and theory for topics relevant to this research project. First, an overview of high-energy radiation production in medical linear accelerators will be presented, along with definitions for absorbed and peripheral doses. The motivation for using FFF beams for VMAT lung SABR will be discussed, and a summary of radiation modelling tools used in this project will be covered.

Chapter 3 will outline the materials and methods used for data collection and analysis. This will discuss the different types of peripheral dose measurements performed, and the tools used for those measurements. The validation of different dose calculation algorithms for peripheral dose prediction will be presented. Finally, the details of the lung SABR study will be introduced.

Chapters 4 and 5 will present and discuss the results of the peripheral dose measurements, the dose calculation algorithm validation, and the lung SABR study. Chapter 6 will present suggestions for future work, and the thesis conclusion.

Chapter 2

Background

This chapter will cover the essential theory for this research project, including the physics of high energy photon production, particle interaction in matter, radiation dose and peripheral dose and radiation modelling.

2.1 The Physics of Radiation Therapy

2.1.1 High Energy Photon Production

Medical linear accelerators and their general components were introduced in chapter 1. Medical linear accelerators produce megavoltage x-rays that are used in radiation therapy for cancer treatment, where typical treatment photons produced by 4 to 25 MV linacs are found in the energy range of less than 100 keV to several MeV [3]. Electrons are accelerated to high energies and then directed onto a metal target to produce bremsstrahlung photons. This photon beam is then further shaped and modulated to deliver an optimal radiation treatment to the patient.

An overview of the electron acceleration and photon production function of a typical high energy medical linac is shown in figure 2.1. The klystron amplifies microwaves to high power, which are funnelled into the accelerator structure by the waveguide. Electrons injected into the accelerator structure are produced by an electron gun, where electrons are "boiled off" a hot cathode. High voltage pulses are supplied to the RF driver and klystron, and simultaneously to the electron gun so that both the klystron-amplified microwaves and electrons are pulse-injected into the accelerator structure at the appropriate time [2]. Within the standing wave accelerator structure, the electron pulse is accelerated by standing RF waves when its

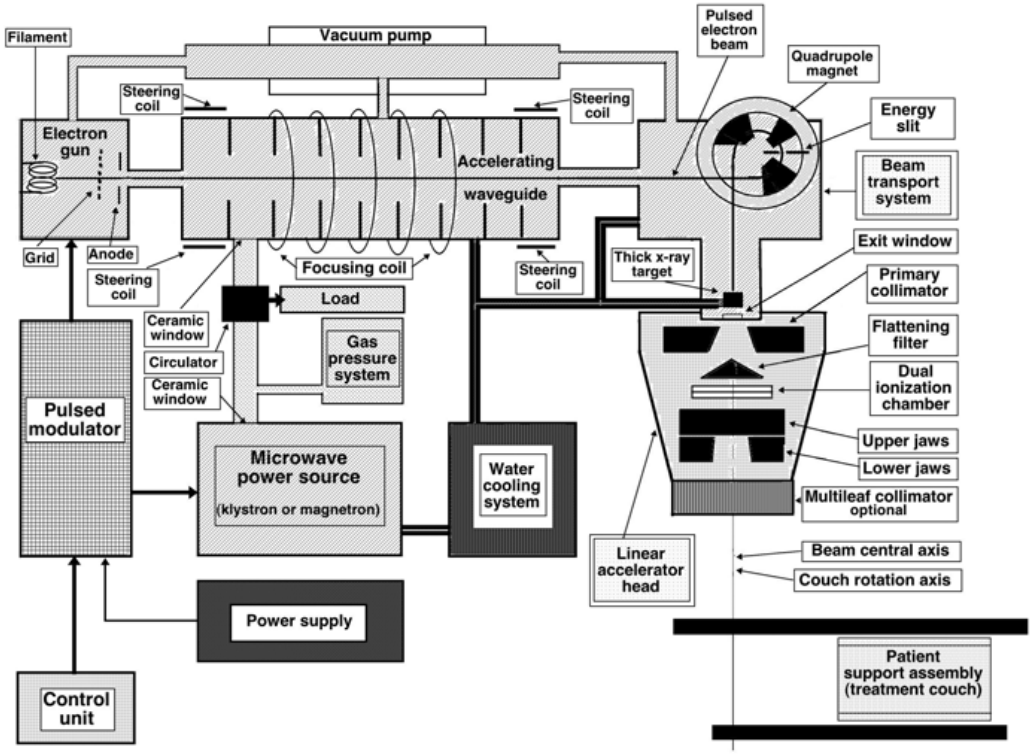

Figure 2.1: Major components of a medical linear accelerator [1]

injection is timed to align with the electric field maxima along the entire trajectory. Electromagnetic steering coils surround the accelerator to maintain the longitudinal path of the electrons.

The electron beam leaves the accelerator structure and enters the bending magnet assembly. Most medical linacs employ a 270° achromatic bending electromagnet, which bends the electron trajectory 270° and focuses the beam to a narrow point, where the metal target is located [22]. The high energy electrons incident on the metal target produce x-ray photons via bremsstrahlung production. Bremsstrahlung photons are produced when a charged particle is negatively accelerated due to interactions with another charged particle. In this process, the accelerated electrons are slowed down by the positively charged nuclei of the metal target. The loss of energy of the electron is manifested as a photon of energy $h\nu$. In addition to the bending magnet assembly, the linac head incorporates lead shielding to minimize radiation leakage.

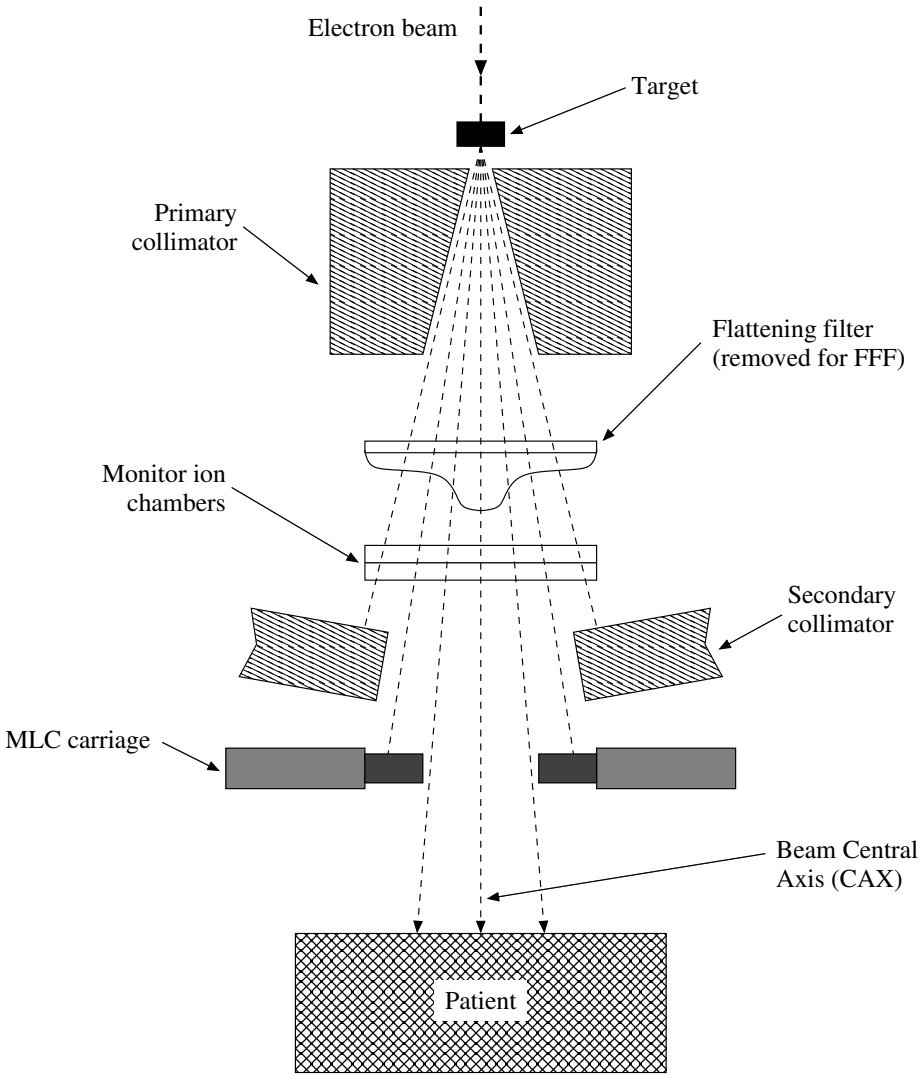

Figure 2.2: Components of a standard medical linac head in photon mode

The beam then passes through several components housed in the gantry head that modify and shape the beam for treatment delivery. Figure 2.2 shows a cross-sectional view of a linac gantry head.

The primary collimator defines the largest field dimension that will be further truncated by the secondary and tertiary collimators as the beam passes through the treatment head.

The flattening filter differentially attenuates the photon beam radially to produce a beam of uniform intensity across the treatment field. A secondary effect of the flattening filter is beam hardening, the preferential absorption of lower energy

photons resulting in a higher mean energy of the filtered beam.

The monitor ion chambers are two independent transmission ion chambers used to measure the machine output and beam flatness and symmetry during radiation delivery. They measure radiation in arbitrary units called monitor units (MU), which are related to dose during the linac calibration. Dose delivery rate is measured in units of monitor units per minute (MU/min). Typically, linacs are calibrated so that 1 MU = 1 cGy at the depth of maximum dose (d_{max}).

The secondary collimators are independent lead "jaws" that define the maximum square or rectangular treatment field size for a given radiation treatment.

The tertiary collimators are additional field shaping devices. On modern machines, multi-leaf collimators (MLC) usually provide the tertiary collimation. The MLC can be used to create irregularly shaped beams specific to a given patient anatomy, and to modulate the radiation intensity across the field for advanced treatment such as IMRT and VMAT.

2.1.2 Dose Deposition

Particle Interactions in Matter

Ionizing radiation incident on an absorbing medium deposits energy into that medium through various processes. There are several interactions that can occur when megavoltage x-ray photons interact with matter (e.g., water or soft tissue), the most significant of which will be described in this section.

Rayleigh Scattering Rayleigh scattering is the elastic scattering of an incident photon through interaction between an atom and an incident photon. Because this is an elastic interaction, no energy is lost to charged particles and no ionizations are produced. Therefore Rayleigh (also known as coherent scattering) does not contribute to absorbed dose [23].

Photoelectric Interactions The photoelectric effect is the ejection of a bound electron from an atom after a collision between the atom and an incident photon, where the photon is absorbed by the atom [24].

Compton Scattering Compton scattering can occur when an incident photon collides with an electron, and transfers energy to the electron. The result is a scattered photon of reduced energy and a corresponding recoil electron.

Pair and Triplet Production Pair and triplet production occur when the energy of an incident photon is absorbed, and subsequently produces a positron-electron pair. This can occur via interaction with the nucleus (pair production), or via interaction with a bound electron, resulting in the positron-electron pair and the original electron (triplet production). Pair production cannot occur for photon energies below 1.02 MeV, and the threshold for triplet production is 2.04MeV[24].

The interactions described above, and the subsequent events are mechanisms of energy transfer to the absorbing medium. When they occur in biological tissue, the scattered electrons and photons from these interactions may then undergo further interactions, losing energy along the way, until all of their energy has been deposited. The relative probability of a given interaction depends on the energy of the incident photons ($h\nu$) and the atomic number (Z) of the absorbing medium. The mean energy of radiation treatment photons are in the MeV range [24], while scattered radiation may have energies as low as the keV range [25].

The amount of interaction or penetration of a beam of incident photons into an absorbing medium is characterized by the linear attenuation coefficient, μ. It is the probability per unit path length that a photon will undergo an interaction with the medium [1]. The total linear attenuation coefficient can be given in terms of the corresponding coefficients for each type of interaction.

$$\mu = \tau + \sigma_R + \sigma + \kappa \tag{2.1}$$

Equation 2.1 gives the total linear attenuation coefficient, where τ, σ_R, σ and κ represent the coefficients for photoelectric, Rayleigh, Compton and pair production interactions, respectively. The individual coefficients are proportional to the cross section for each interaction, while μ (in units of cm^{-1}) is proportional to the cross section of any interaction occurring. The attenuation coefficient is often shown as the mass attenuation coefficient, $\frac{\mu}{\rho}$ (cm^2/g).

Figure 2.3 shows the total mass attenuation coefficient for carbon ($Z = 6$), as well as the contributions made by the different interactions at different energies. The

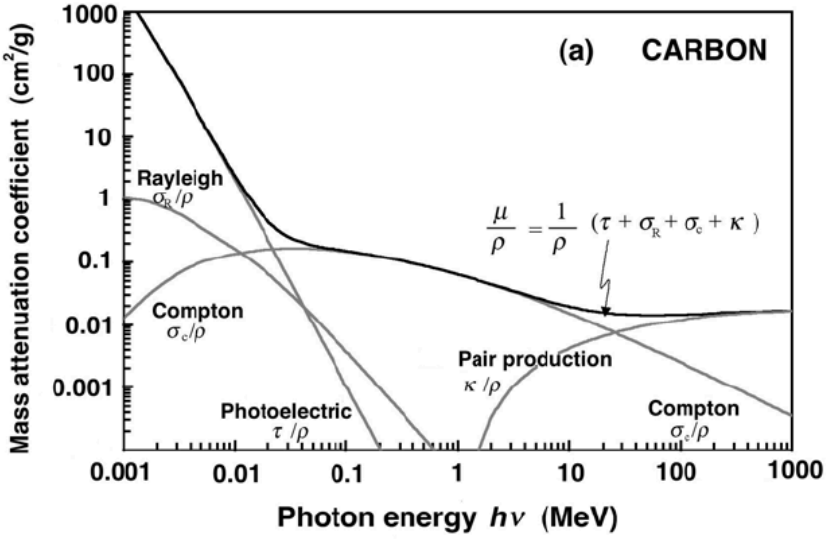

Figure 2.3: Contributions of each component of the mass attenuation coefficient in carbon [1].

mean energy of a typical radiation therapy beam is found in the 1 to 10 MeV range, where Compton scattering has the largest contribution.

The dominant interaction at different energies is summarized for a range of Z materials in figure 2.4. In this project, treatments using beam energies of 6 to 10 MV will be studied. For the majority of the range of energies for in-field and scattered radiation for these treatments, Compton scattering is the dominant interaction.

A related quantity to the mass-attenuation coefficient is the mass-energy transfer coefficient, which describes the net energy transferred through interaction with the medium. This quantity, $\frac{\mu_{tr}}{\rho}$, is given by,

$$\frac{\mu_{tr}}{\rho} = \frac{1}{\rho}\left(\tau_{tr} + \sigma_{tr} + \kappa_{tr}\right), \tag{2.2}$$

where $\frac{\tau_{tr}}{\rho}$, $\frac{\sigma_{tr}}{\rho}$ and $\frac{\kappa_{tr}}{\rho}$ represent the energy transferred to the absorbing material by each type of interaction. The coefficient for Rayleigh scattering here is not included, because it does not transfer energy to the medium.

The energy transferred to the medium will not always be entirely absorbed, some energy being lost by bremsstrahlung production and in-flight annihilation [23]. The energy absorbed by the medium per unit mass is given by the mass energy-absorption coefficient, $\frac{\mu_a}{\rho}$.

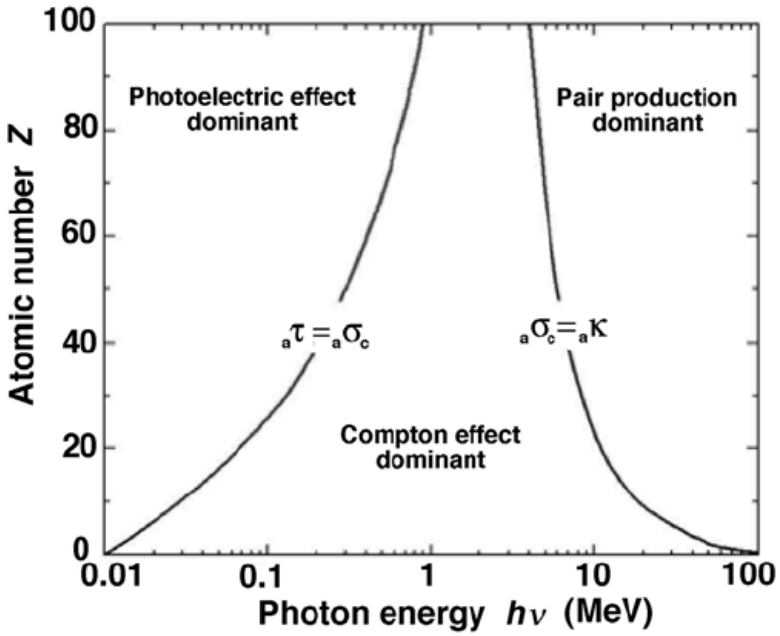

Figure 2.4: Relative importance of different interactions according to photon energy and atomic number [1].

$$\frac{\mu_a}{\rho} = \frac{\mu_{tr}}{\rho}(1-g), \tag{2.3}$$

where g is the average fraction of secondary-electron energy lost by bremsstrahlung production or in-flight annihilation.

Absorbed Dose

The dose absorbed by matter through interactions with ionizing radiation is defined as the expectation value of the energy imparted to matter per unit mass at a given point [23]. This is given in equation 2.4,

$$D = \frac{dE}{dm}, \tag{2.4}$$

where dE/dm is the energy imparted per unit mass, and D is the dose measured in Gray (Gy), where 1 Gy = 1 J/kg. In radiation treatment planning and delivery, all doses are given in units of Gy or cGy, where 1 Gy = 100 cGy.

Radiobiology

Biological tissues respond to radiation in different ways, depending a number of factors, including dose received and organ volume irradiated. Normal and malignant tissues exhibit different responses to radiation exposure, and these differences are exploited in radiation therapy. A curative radiation treatment is designed to deliver enough dose to the malignant tissue to achieve local control (the prevention of tumour regrowth during the lifetime of the patient [3]), while allowing normal tissues to recover from the unavoidable exposure they receive over the course of the treatment.

Common side effects of radiation therapy treatments include early and late normal tissues responses, as well as the induction of secondary cancers. Early effects occur within the first three months of radiation treatment and include effects in highly proliferative tissues, such as the skin and oral mucosa [3]. Late effects occur outside of the three month period and may present at any time over the lifetime of the patient. These include changes to endothelial, parenchymal and connective tissues, which eventually result in a loss of function within the irradiated volume [3].

The last side effect caused by dose received by normal tissues is carcinogenesis. The same mechanism used in radiation therapy to kill malignant cells can increase the probability of cancer development in normal cells. If a cell's DNA is damaged, but does not trigger cell apoptosis (cell death), the still-viable cell may cause a malignancy down the line. The appearance of secondary cancers after radiotherapy has been observed even in tissues receiving relatively low doses, and it is generally accepted that in terms of cancer induction, no dose is too small to be effective [26].

2.1.3 Peripheral Dose

The peripheral dose associated with radiation therapy is defined as the dose received by tissues outside of the treatment field. Peripheral doses have been an area of concern in radiation therapy for many years due to the potential risk of secondary cancer development, as well as other factors such as heart disease, stroke and the risk to the fetus for treatment of pregnant women [16, 27, 28]. There exists a large body of published work that attempts to measure, model and quantify peripheral doses for different radiation treatments, and the risk of secondary cancers associated with them [15]. One study of secondary malignancies in people treated with radiotherapy for childhood cancers found that peak frequency of secondary malignancies was found in tissues receiving less than 2.5 Gy, and that these secondary cancers appeared over

the range of 5 to 40 years after treatment [14].

The emergence of highly modulated treatments such as IMRT and VMAT has increased the risk of secondary cancers, as compared to conventional radiotherapy [16, 29, 30]. This is caused by an increase in peripheral dose due to the increased scattered radiation arising from the treatment head, as well as the increased number of MUs (and therefore beam-on time) delivered per treatment.

There are three main sources of radiation contributing to out-of-field dose, including head scatter, patient scatter and treatment head leakage [11]. Head scatter includes any radiation scattered from beam-shaping component of the treatment head, such as the flattening filter, secondary and tertiary collimators. Patient scatter includes radiation scattered internally within the patient from the primary beam. Finally, treatment head leakage includes leakage through the accelerator head shielding [11]. Each component of peripheral contributes to the peripheral dose at all points outside of the field, but the relative importance of these components changes depending on energy, depth in the patient, and field size. In general, head scatter dominates the peripheral dose at small distances from the edge of the treatment field [21]. Patient scatter dominates in the intermediate range, and treatment head leakage dominates the peripheral dose at distances of 15-30 cm from the edge of the field [11, 13, 21].

The peripheral dose is difficult to assess for a number of reasons. First, the energy spectrum of radiation in the peripheral region is significantly lower (estimated to be in the 0.2-0.6 MeV range for a 6 MV beam) than the energy spectrum of the primary beam [21]. This poses problems for measurement of the dose, because many commonly used dosimeters such as radiochromic film and thermoluminescent dosimeters (TLDs), are known to over-respond to low energies [23, 31]. Ion chamber response is known to be relatively flat, however the measurement of peripheral doses using one ion chamber can be time-consuming. Furthermore, the relatively low number of particles in this region results in a higher statistical uncertainty.

For the above reasons, as well as the fact that one cannot measure the dose inside of a real patient, assessing peripheral dose through computational means is an attractive alternative. However, many existing dose calculation algorithms are designed for in-field dose calculation, and some approximations used in these calculations result in decreased accuracy in the out-of-field region.

2.2 Flattening Filter Free (FFF) Beams

Medical linacs produce high energy photons via bremsstrahlung production, when a high speed beam of electrons is directed at a metal target. Bremsstrahlung photons are emitted in a continuous spectrum of energy, where the maximum possible energy is the incoming electron's total energy, and the emission angle of a given photon is dependent on its energy. Therefore, photon beams produced in linacs have non-uniform energy and angular distributions [22]. The angular distribution of bremsstrahlung photons depends on the initial kinetic energy of the electron beam. In general, the higher the electron kinetic energy, the more forward peaked the resulting bremsstrahlung intensity profile. For example, the angle of peak bremsstrahlung photon intensity (with respect to the initial electron trajectory) for 10 MeV electrons is 1.4°, while it is approximately 64.4° for a 10 keV beam of electrons [1]. Medical linac photons beams are usually designated in terms of the electron beam kinetic energy. For example, a standard 6 MV photon beam has a maximum photon energy of 6 MeV, while its mean energy is approximately 2 MeV, or one-third of the maximum [2].

Historically, flattening filters have been employed in medical linacs to create a relatively uniform photon fluence profile for standard photon beams. Flat beams were necessary to make early treatment planning calculations feasible. With the advent of computerized treatment planning systems that calculate dose for non-uniform intensity modulated beams, the need for a flattening filter was eliminated.

As discussed above, bremsstrahlung photons are forward peaked, meaning that they have a higher intensity on the central axis of the beam. Flattening filters are cone-shaped, in order to attenuate the forward-peaked high intensity part of the photon beam more than the beam edges. Figure 2.5 compares the dose rate for a flattened 6 MV and unflattened 10 MV photon beam. These profiles were measured at a depth of 10 cm, but to illustrate the difference in dose rate they were normalized to reflect the dose rate at d_{max}. The high intensity along the central axis of the unflattened beam is apparent.

In general, FFF beams portray several distinct characteristics, as compared with standard flattened beams.

- High central axis intensity and dose rate: The high intensity bremsstrahlung peak is not attenuated to match the intensity of the outer regions, so it maintains a higher dose rate [32]. For example, on the Varian TrueBeam (Varian Medical

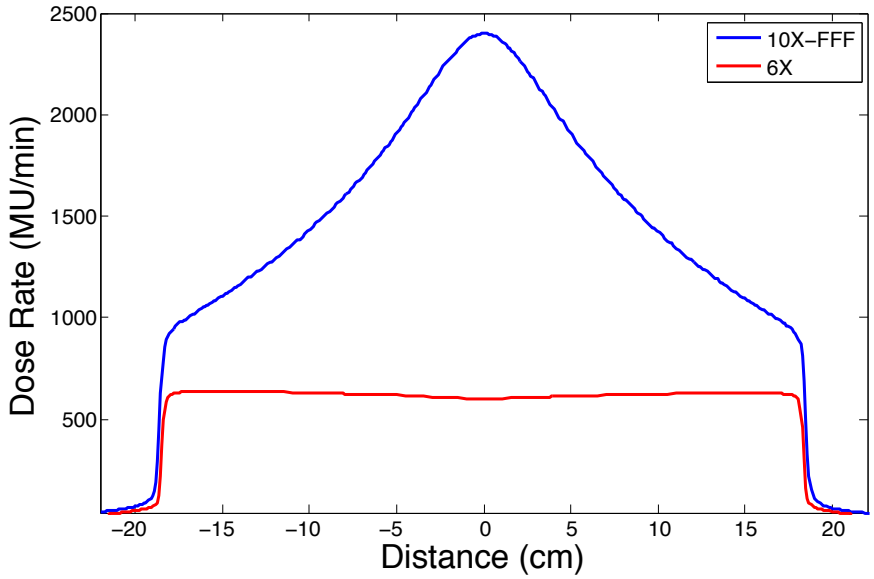

Figure 2.5: FFF vs FF beam profiles for an open field.

Systems, Palo Alto, CA), FFF beams can be delivered at 2400 MU/min, while the highest dose rate for flattened beams is 600 MU/min.

- Lower mean energy: A side-effect of flattening the photon beam is that the lower energy photons are attenuated more than the higher energy photons (due to a higher interaction cross-section), making the mean energy of the resulting beam higher. This is a phenomenon known as beam hardening. With the absence of beam hardening, FFF beams have lower mean energies than their flattened counterparts [33, 32]. For example, a 10 MV FFF beam has a mean energy approximately equivalent to an 8 MV flattened beam.

- Reduced head scatter: Approximately one-third of all head scatter present in flattened beams is created in the flattening filter. The removal of the flattening filter significantly reduces the scatter associated with the photon beam [33].

- Reduced MLC leaf transmission and MLC leakage radiation compared to flattened beams [34, 10].

2.2.1 Motivation for the use of FFF beams for Lung SABR

FFF beams have been investigated for several different types of SABR treatments for several reasons. The high does rate available with FFF beams allow for shorter treatment times, which reduces intra-fractional patient and organ motion. A reduction in treatment time would be particularly advantageous for lung SABR, where typical treatments with unflattened beams take 5-7 minutes of beam-on time due to the high dose per fraction. One study found that average beam-on times were reduced by a factor of up to 2.5 for FFF deliveries [17]. As well, FFF beams have been shown to deliver dosimetrically equivalent plans, as compared to flattened beams [18, 19, 17, 20].

An additional potential benefit of the use of FFF beams for VMAT lung SABR plans is the reduction in peripheral dose. Due to the reduction in treatment head scatter and MLC leaf leakage and transmission demonstrated by FFF beams, the out-of-field scatter and therefore dose, is reduced. Also, due to the beam-on time reduction, the treatment head leakage will also be smaller for FFF beam, for a given treatment. Reductions in peripheral dose for FFF beams have been demonstrated for small conformal fields and IMRT treatments for various treatment sites [35, 21].

2.3 Radiation Beam Modelling

This section will discuss the treatment planning process as well as the different dose calculation algorithms used in this project.

2.3.1 Treatment Planning System

Radiation Therapy treatment planning is a complex procedure that involves a team of medical physicists, radiation oncologists and radiation therapists. Treatment planning involves first the acquisition of a planning CT image, which gives the patient's anatomical geometry and density information. The image is then contoured, which means that critical structures are outlined. These structures include the planning target volume (PTV), organs at risk (OARs), and certain other structures that are used to assess plan quality. The PTV is a volume that encompasses the tumour plus a given margin designed to account for set up and delivery error and the the potential presence of cancerous cells around the tumour periphery, and OARs are sensitive organs that are generally located directly adjacent to the radiation field.

Once the structures are contoured, the treatment plan is designed. There are two types of planning used in radiation therapy, forward and inverse planning. Forward planning is the method used historically, and is still used to plan certain types of treatments. This method requires the radiation fields to be set up first by the treatment planner, before dose calculation. This is a well-understood method, but is only possible for simple types of treatments.

Inverse planning is a method used for treatment planning of more complex treatments such as IMRT and VMAT. Inverse planning requires the input of certain plan parameters, such as prescription dose, dose limits to the PTV and OARs, and MU constraints. The plan optimizer then minimizes an objective function to arrive at a possible plan that meets the input parameters.

Once the physical plan parameters have been reached by optimization, the dose is calculated. This can be achieved with various different methods of modelling the dose deposition process. A true simulation would use the Monte Carlo (MC) method (discussed later in this chapter), however the long computation time associated with MC calculations limits its practical applicability within treatment planning system. Generally, faster dose calculation algorithms are used by commercial treatment planning systems.

The treatment planning system used in this project is the Eclipse$^{\text{TM}}$ Treatment Planning System, version 11 (Varian Medical Systems, Palo Alto, CA). The dose calculation algorithms available within Eclipse are the Analytical Anisotropic Algorithm (AAA) and the Acuros® XB algorithm for external beam photon dose calculation.

AAA

AAA is a 3D pencil beam convolution/superposition algorithm that uses Monte-Carlo derived primary and secondary photon source models. AAA divides the beam into smaller "beamlets," β, whose size is determined by the dose calculation grid resolution in the isocenter plane. The dose calculation is accomplished by first performing a convolution over the beamlet cross-sections separately for primary photons ($ph1$), scattered photons ($ph2$), and contaminating electrons ($cont$). These convolutions give an energy distribution for each beamlet at a given point (X, Y, Z) in the patient. The final energy distribution is a superposition of the contributions from each of the convolutions, as shown in equation 2.5.

$$E(X,Y,Z) = \sum_{\beta}(E_{ph1,\beta}(X,Y,Z) + E_{ph2,\beta}(X,Y,Z) + E_{cont,\beta}(X,Y,Z)) \tag{2.5}$$

The energy distribution is then converted to the final dose distribution using the scaled water approximation.

$$D(X,Y,Z) = cE(X,Y,Z) \cdot \frac{\rho_{water}}{\rho(X,Y,Z)}, \tag{2.6}$$

where c is a constant used to convert the dose into units of Gy, ρ_{water} is the density of water, and $\rho_{(X,Y,Z)}$ is the density of the medium at that point.

AAA has some known limitations, namely that it tends to overestimate dose in low-density tissues (lung), and that it underestimates the out-of-field dose [36, 37].

Acuros XB

Acuros XB is an algorithm used for accurate dose calculation for photon beams, especially for plans containing heterogeneous tissue densities. Both AAA and Acuros XB use the same Monte Carlo-derived photon source model for their calculations. Acuros XB solves the linear Boltzmann transport equation (LBTE), which describes the macroscopic behaviour of radiation when it interacts with matter. Acuros XB was intended to be a faster alternative to Monte Carlo simulations, but an improvement over AAA for dose calculation in non-homogeneous tissues [36].

The Acuros XB dose calculation occurs over a series of five steps:

1. Construction of a physical material map, based on the mass density of the material (given by the CT image), and the cross sections for different interactions (photoelectric, Compton, etc.).

2. Transport of the components of the photon sources models into the patient. These source models include the primary and secondary photons and contaminating electrons.

3. Transport of the scattered photon fluence in the patient

4. Transport of the electron fluence in the patient.

5. Dose Calculation based on the previous four steps. Once the electron angular fluence, $\Psi_e(\vec{r}, E)$, has been calculated, the dose, D_i, deposited in a given voxel, i, is calculated according to,

$$D_i = \int_0^\infty dE \int_{4\pi} d\hat{\Omega} \frac{\sigma^e(\vec{r}, E)}{\rho(\vec{r})} \Psi_e(\vec{r}, E), \tag{2.7}$$

where σ^e is the energy deposition cross section in MeV/cm and ρ is the material density in g/cm^3.

Acuros XB has been shown to be an improvement over AAA for dose calculation at the lung-soft tissue interface. It has also demonstrated faster calculation times for VMAT calculations, but longer calculation times for IMRT calculations [38].

2.3.2 Monte Carlo System

The Monte Carlo method will be discussed in this section, as well as the BC Cancer Agency's web MC system used in this project.

The Monte Carlo method

The Monte Carlo method is a numerical technique used to calculate probabilities and other related quantities using random numbers [39]. A sequence of random numbers, $r_1, r_2, ...r_n$, is used to determine another sequence of values, $x_1, x_2, ...x_n$, that are distributed according to a probability distribution function (pdf). This is a method of randomly sampling from the pdf which governs the real phenomenon that is being simulated.

MC can be used to accurately model radiation transport, and is used for many applications in medical physics. The most relevant application of MC to this project is the simulation of patient treatment and dose deposition. The general process to for modelling radiation transport first requires information about the incoming particles, including the particle type, position, direction and initial energy. Given each particle's information, the distance to the particle's next interaction is determined, based on the exponential pdf of attenuation in a particular medium. Next, the type of interaction is determined based on the cross sections (ie: Compton scattering, photoelectric effect, etc). The new energy and direction of the particle are determined based on the type of interaction, and the transport of any secondary particles produced by this interaction

is then modelled in the same way. When simulating radiation transport of particles through the treatment head, it is often useful to score quantities of interest, such as the particle spectrum, over several different histories, or cases. For dose deposition, the dose is averaged over volume elements (voxels) of a finite size [40].

Monte Carlo system

EGSnrc is a system of computer codes used for MC modelling of photon and electron transport [41]. BEAMnrc [42] is a MC simulation package, built on the EGSnrc system, used to model radiation therapy beams. Similarly, DOSXYZnrc is an EGSnrc - based MC simulation system, used to calculate the dose deposition in matter [43]. The MC system used for radiation therapy simulation at the BC Cancer Agency is built on these code systems.

Due to the complexity of radiation interaction with matter, MC generally requires long calculation times, as compared to other dose calculation algorithms. However, many techniques have been developed to optimize MC for radiotherapy applications that have improved calculation efficiency [40]. Figure 2.6 shows a representation of the relevant steps involved in the simulation of treatment plans in this project. Included are the different codes used in the MC system to increase MC efficiency for clinical treatment plan verification.

A full radiation therapy simulation would include a full BEAMnrc simulation of the particle source [42]. However, for simulation of a photon beam from the Varian Truebeam (Varian Medical Systems, Palo Alto, CA), the company-supplied phase space (source model) must be used. A phase space describes the particle types, energies, positions, directions and fluences. The input phase space for these simulation is above the patient-specific linac head components (secondary collimators).

Next, the simulation of particle transport through the linac head components is performed. The first plan-specific component is the secondary collimator, known as the linac jaws. BEAMnrc codes include a real simulation of the linac jaws, including particles scattered from the jaws. The other collimator model is the Phase space Collimation. This jaw model decreases calculation time by eliminating particles that do not fall within the open field defined by the jaws. Therefore, no scatter is modelled when using Phase space Collimation, but calculation times are reduced.

The MLC is then modelled by either the dynamic Varian MLC (DYNVMLC) model [42], or the Virginia Commonwealth University dynamic MLC (VCU DMLC)

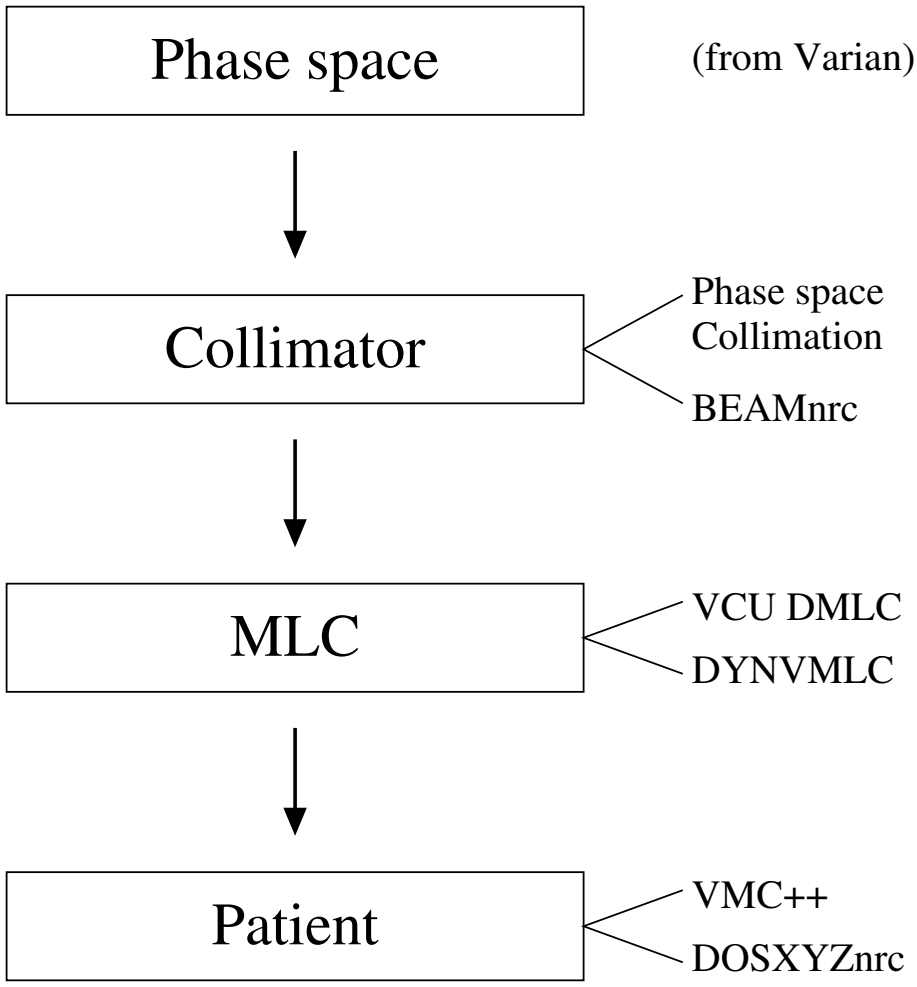

Figure 2.6: An explanation of the webMC system

model [44]. The DYNVMLC does a true MC simulation of the MLC, which can be time consuming due to the complexity of the leaf motions during treatment. The VCU DMLC model was designed to be an accurate and more efficient alternative to the full simulation, and has been found to give very accurate in-field results [44].

A phase space is scored for each plan after the linac head simulation, and fed to the dose engine. In this project, the dose engines used were either DOSXYZnrc, which is the EGSnrc-based code that simulates dose deposition in a medium. DOSXYZnrc uses CT data to generate material densities used in the calculation [43]. VMC++ is an alternative dose engine that was designed to increase the calculation efficiency of DOSXYZnrc. There are several differences made in VMC++ as compared to DOSXYZnrc. VMC++ uses the STOPS technique, which groups particles produced

by the same interaction (ie: Compton electrons) together in particle sets for transport. It also makes some changes to the simulation of low energy particles compared to DOSXYZnrc [45]. In DOSXYZnrc, electrons below the cutoff energy are deposited as dose at that point, but in VMC++, electrons below the cutoff are slowed down to zero energy in two steps [45].

2.4 Summary

This chapter has described the concepts necessary for the remainder of this research project, including the physics of radiation therapy, flattening filter free (FFF) beams, and radiation modelling techniques. The physics of high-energy photon production and the interaction of photons with matter were discussed. The concept of absorbed dose was introduced, as well as an explanation of peripheral doses and their consequences. The characteristics of FFF beams were presented and discussed in the context of VMAT lung SABR treatments. Finally, an overview of radiation modelling was discussed. This included a description of treatment planning, including different dose calculations, and Monte Carlo modelling. An overview of the specific Monte Carlo system used in this project was given.

Chapter 3

Materials and Methods

The peripheral doses delivered by VMAT Lung SABR treatments were systematically investigated for both FFF beams and flattened beams. Three energies were chosen for this study: 10X-FFF, 10X and 6X. VMAT Lung SABR treatments at the BC Cancer Agency are generally delivered using the flattened 6X mode, while the available flattening filter free mode was 10X-FFF. The 10X flattened beam was used for a direct comparison of flattened and unflattened beams of the same energy.

This project was divided into three components:

1. Ion chamber measurement of peripheral dose for three types of plans.
2. Validation of Monte Carlo, Acuros XB and AAA algorithms for peripheral dose prediction using measured data.
3. Use of the validated Monte Carlo model to evaluate peripheral doses for VMAT lung SABR treatments.

Components 1 and 2 were performed using a progression from simple to complex fields, which were planned using the Eclipse^{TM} Treatment Planning Software (TPS) (Varian Medical Systems, Palo Alto, Ca). They included:

Static Open Fields: square fields defined by the secondary collimators.

Static MLC Fields: square fields defined by a static MLC shape.

Dynamic MLC Fields: fields modulated by the MLC.

These fields were delivered with a static gantry position, with a gantry angle of 0° for static open and static MLC fields, and 315° for dynamic MLC fields. Figure 3.1 shows a beam's eye view of each type of field, and their respective dose distributions.

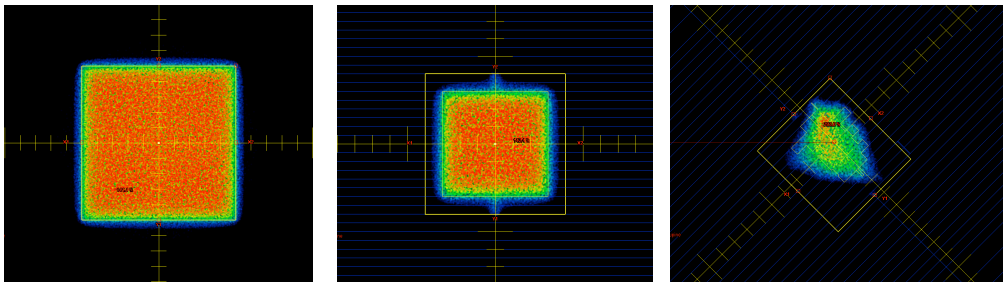

(a) Static Open Field (b) Static MLC Field (c) Dynamic MLC Field

Figure 3.1: Beam's Eye View of the three types of fields

3.1 Ion Chamber Measurements

Dose measurements were performed using a 0.6 cc Farmer ion chamber (PTW-Freiburg, Germany) in a $30\times20\times60$ cm^3 solid water phantom. All measurements were performed on the Varian Truebeam linac equipped with the Millennium 120 MLC (Varian Medical Systems, Palo Alto, CA). Dose measurements were performed from the central axis (0 cm), to a position 36 cm from the central axis for varying field sizes, measurement depth and treatment couch orientation, as shown in table 3.1.

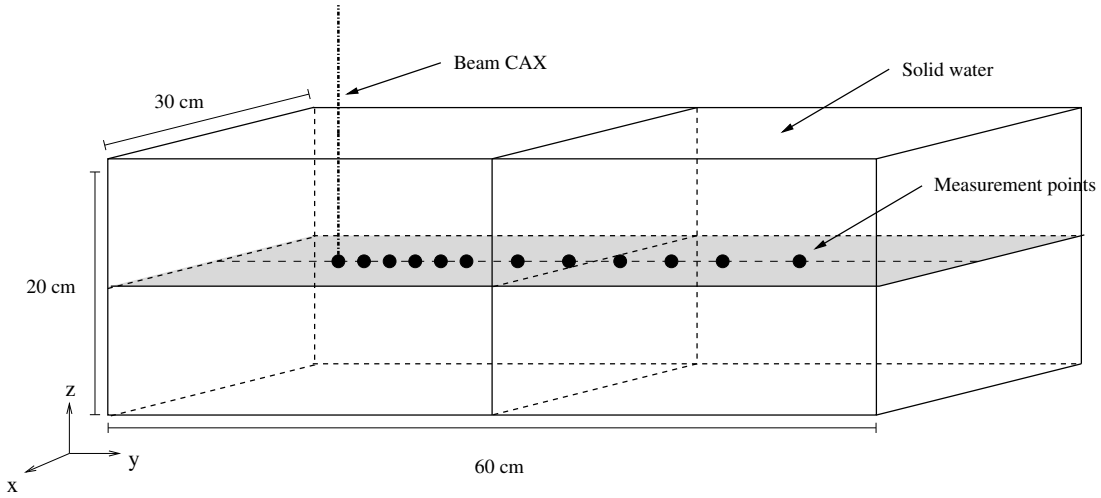

Figure 3.2: Solid water phantom used for peripheral dose measurements

The spatial resolution of measurement points was 2 cm, 4 cm or 6 cm, depending on the region (a higher spatial resolution was used for the higher dose gradient regions). The solid water phantom and measurement point spacing for a typical peripheral dose measurement is shown in figure 3.2. In-Plane (IP) is defined as the y-plane (the y jaws move in the y plane when the collimator rotation is 0°), and

Cross-Plane (CP) is defined similarly as the x-plane. A set of measurements was taken for each field and each of the three energies. A beam's eye view of the measurement set-up in relation to the in-plane (y) and cross-plane (x) is shown in figure 3.3.

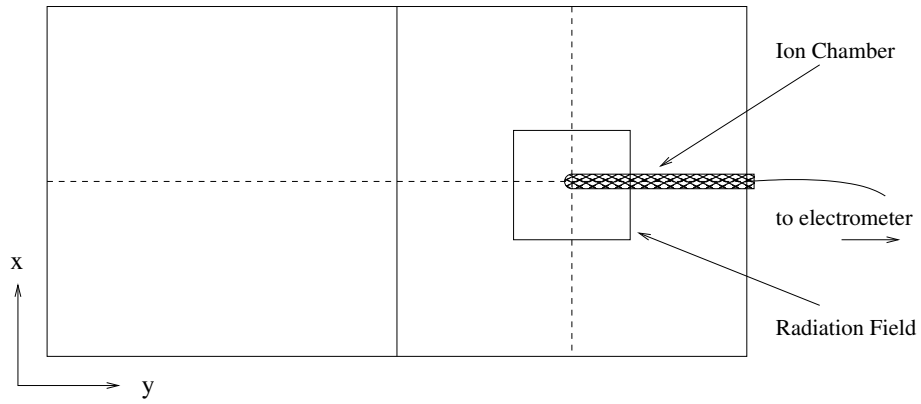

Figure 3.3: Beam's eye view of the measurement setup.

Measurement were performed only in the IP direction for dynamic MLC fields, because a collimator setting of 315° would greatly minimize any IP/CP differences in dose. An additional set of measurements was taken for the dynamic MLC fields, using a solid water phantom with low density plastic "lung" inserts. Figure 3.4 shows the dimensions of the inhomogeneous phantom.

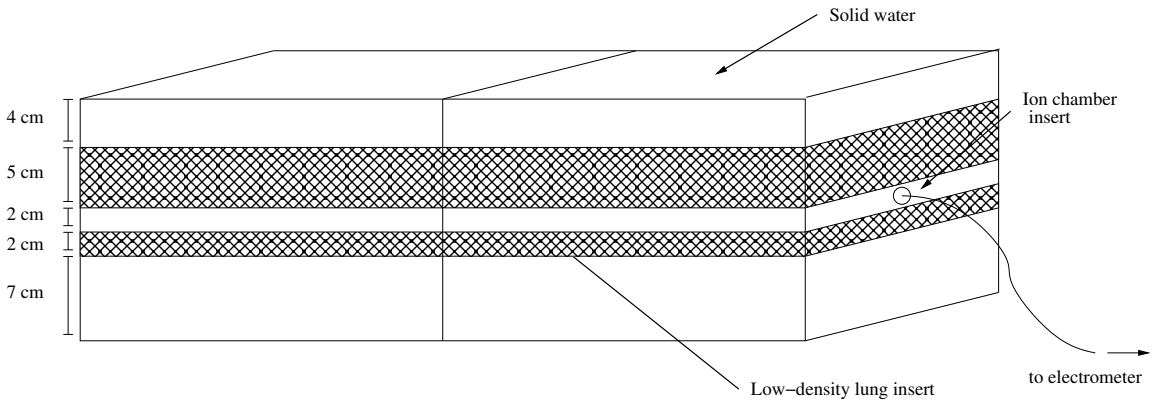

Figure 3.4: Solid water phantom with low-density lung insert

The 6X and 10X fields were delivered at a dose rate of 600 MU/min and the 10X-FFF fields were delivered at 2400 MU/min, each corresponding to the highest dose rates available for the given energy. The in-plane setup is shown in figure 3.5.

Type of Field	**Field Size (cm^2)**	**Measurement Depth (cm)**	**Orientation**	**Energy**
Static Open	5×5, 10×10	5, 10	IP, CP	10X-FFF, 10X, 6X
Static MLC	6×6 (MLC)	10	IP, CP	10X-FFF, 10X, 6X
Dyn MLC	-	5	IP	10X-FFF, 10X, 6X
Dyn MLC + Lung	-	10	IP	10X-FFF, 10X, 6X

Table 3.1: Peripheral dose measurement parameters

Ion chamber measurements were normalized to the corresponding central axis (CAX) measurement and are presented in terms of percentage of the CAX dose. CAX measurements were taken periodically during data collection, to minimize the effect of temperature and pressure variations.

An ion recombination correction factor (P_{ion}) was applied to all measurements. P_{ion} corrects for the incomplete collection of charge in an ion chamber. This is of particular concern for 10X-FFF, due to the availability of high dose rates (high dose per pulse) for FFF beams. P_{ion} was measured for each energy at specific intervals along the measurement plane, using the two-voltage technique described in the Task Group 51 (TG-51) protocol [46]. The two-voltage technique has been shown to adequately account for ion recombination for high dose rate FFF beams on the Varian TrueBeam (P_{ion} remains < 1.05) [47]. This technique involves measuring the charge produced in the ion chamber at two different ion chamber bias voltages, V_H and V_L, for the same radiation beam. For this project, 300 V and 150 V were used as V_H and V_L, respectively. Equation 3.1 was used to calculate P_{ion},

$$P_{\text{ion}}(V_H) = \frac{1 - V_H/V_L}{M^H_{\text{raw}}/M^L_{\text{raw}} - V_H/V_L}, \tag{3.1}$$

where M^H_{raw} and M^L_{raw} are the raw charge measurements for the high and low bias voltages. For all energies, P_{ion} was found to be in the range of 1.000 - 1.003 outside of the field. Inside the field, P_{ion} for 10X-FFF was found to be 1.012, while for 6X and 10X it remained unchanged, which is in agreement with the current literature [47].

The mean energy in the peripheral dose region is notably lower than the mean energy of the incident radiation beam [21]. While the primary beams have mean energies of approximately 2 MeV to 4 MeV, some Monte Carlo calculations estimate

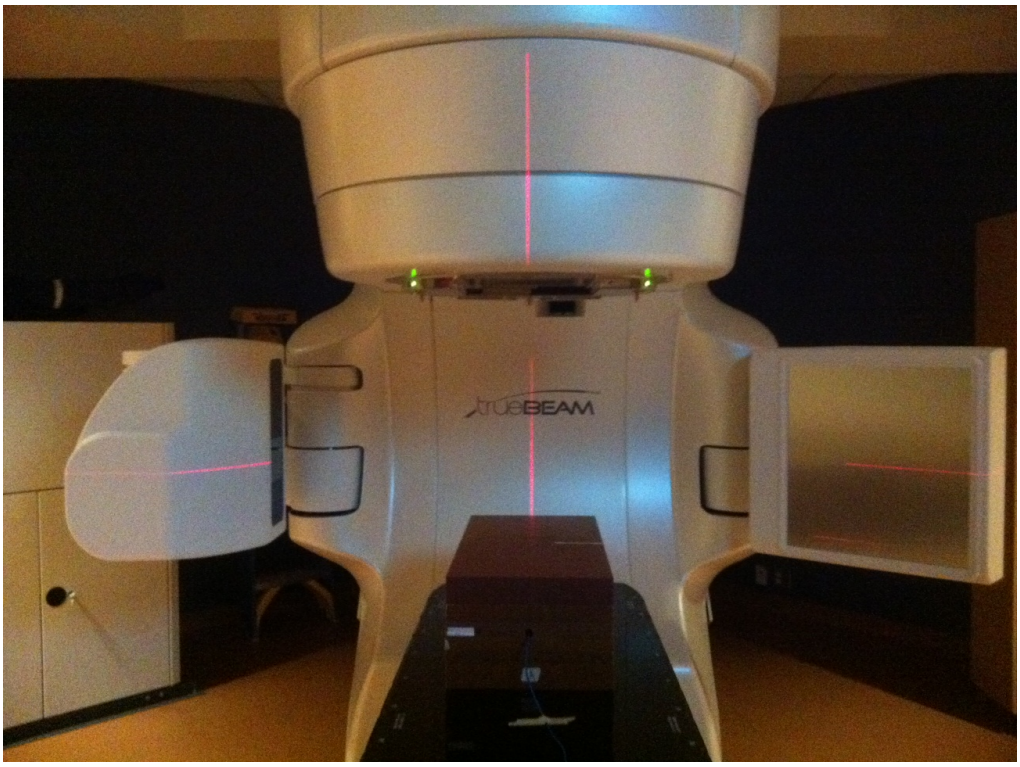

Figure 3.5: In-plane ion chamber measurement setup, including the ion chamber in the solid water phantom and the Varian TrueBeam with gantry and treatment couch each positioned at 0°. The lateral and sagittal setup lasers are also shown. The solid water is positioned at 90 cm SSD, and the ion chamber is at a depth of 10 cm in solid water.

the mean energy outside of the field to be on the order of 0.2 MeV - 0.6 MeV [21]. This difference in energy is not thought to significantly affect the results, since the detector response is relatively energy independent [25]. The change in detector response associated with the difference in energy between the in-field and out-of-field regions is estimated to be less than 1% [25].

The positional uncertainty in the measurement plane was estimated to be a maximum of 2 mm, when accounting for machine quality control tolerances for couch, laser, optical distance indicator and crosshair position, and user setup error. An overall uncertainty of 3 to 10% was estimated for these measurements using $\sigma_{\text{tot}} = \sqrt{\sigma_{\text{tp}}^2 + \sigma_{\text{e}}^2 + \sigma_{\text{p}}^2}$, where σ_{tp} is the uncertainty due to temperature and pressure variations, σ_{e} is the uncertainty in the measured value given by the ion chamber/electrometer setup, and σ_{p} is the uncertainty in the dose due to random positional uncertainty.

3.2 Validation of Monte Carlo, Acuros XB and AAA Algorithms for Peripheral Dose

All fields were planned using Eclipse TPS. Several dose calculation algorithms were used to calculate the dose inside and outside of the fields. The dose calculated by each algorithm was compared to the measured data, in order to evaluate the dose calculation algorithms for peripheral dose prediction.

Within Eclipse, two dose calculation algorithms were used; the Anisotropic Analytical Algorithm (AAA) version 11.0.31, and the Acuros External Beam Algorithm (Acuros XB) version 11.0.31. In addition to the Eclipse algorithms, the BC Cancer Agency's MC system, described in chapter 2, was evaluated and several versions of the system (made of up different components) were used. The following list is a summary of all dose calculation algorithms evaluated, and a short description of each.

Eclipse TPS

AAA AAA was described in chapter 2, and is the current standard for dose calculation in Eclipse at the BC Cancer Agency.

Acuros XB is a more recently implemented dose calculation algorithm, and at the time of data collection, was not yet commissioned for clinical dose calculation at the BC Cancer Agency.

Monte Carlo

Quick MC: The most simplified version of MC tested. Quick MC uses phase space collimatiom, the VCU DMLC model, and the VMC++ dose engine to reduce calculation time.

Advanced MC: The more complex version of MC tested. Advanced MC does a true simulation of the collimator jaws (BEAMnrc collimator), and uses the DOSXYZnrc dose engine for dose deposition in the patient or phantom. Two different MLC models were used with Advanced MC: the **VCU DMLC** model [44], and the **DYNVMLC** model [42].

AAA and Acuros XB plans were calculated within the treatment planning software, and exported from Eclipse for calculation in MC. The voxel size (dose grid) for

AAA and Acuros XB calculations was $(0.25\ \text{cm})^3$, and $(0.5\ \text{cm})^3$ for MC. All calculated dose was reported as dose to water. All plans were run with a total (in-field) uncertainty of 0.5% - 0.1%, which gives statistical uncertainties given by the MC-generated uncertainty matrix in the peripheral region on the order of 10% - 20% of the local dose. These uncertainties are calculated using a standard batching technique, described in [43] and [48]. MC calculated dose files were downloaded directly from the MC system itself. Analysis was performed in MATLAB® version 2012a (Mathworks, Natick, MA, USA).

3.3 VMAT Lung SABR Study

The VMAT Lung SABR study was a comparison of the peripheral doses for six VMAT lung SABR cases calculated with the validated MC model.

Treatment cases were selected for this study based on Planning Target Volume (PTV), to include a representative sample of the range of volumes generally treated with VMAT lung SABR. Each case was planned for 6X, 10X and 10X-FFF (6 cases $\times$ 3 energies = 18 plans in total). The number of MU's was restricted for the three plans for each case to within 10% of each other, in order to minimize the variation in the radiation leakage component of peripheral dose. Restricting the number of MU's for a VMAT lung SABR plan would not be done clinically; the plan which gives the optimal dose distribution would be chosen. However, it was done in this study in order to compare the peripheral dose for the same number of MU's between beam energies. For clinically relevant comparisons, the relative number of MU's required for plans of each energy to achieve the same dose distribution should be considered.

Each plan followed the *Protocol Guidelines for Stereotactic Body Radiotherapy (SBRT) for Primary Early Stage NSCLC in British Columbia* [9]. The prescribed dose for each plan was 48 Gy in 4 fractions, with dose delivered in one arc per fraction. The PTV volume and average number of MU for each case are shown in table 3.2. Analysis for this section was performed in MATLAB® version 2012a (Mathworks, Natick, MA, USA).

3.3.1 Monte Carlo Simulations - Static Gantry Delivery

In order to evaluate the peripheral dose associated with these VMAT lung SABR plans, the measurement and MC validation components were performed with a static

Case #	PTV vol (cm^3)	MU		
		6X	10X	10X-FFF
1	141.20	2893	2797	2823
2	101.40	3952	3874	4115
3	76.30	4261	4172	4320
4	42.40	4102	4125	4399
5	28.15	4008	4283	4401
6	11.20	3395	3624	3690

Table 3.2: PTV volume and average number of MU for each case.

gantry position. The MC system was limited to static gantry positions (VMAT calculations not yet available) at the time of data collection for the majority of this project, thus the previous sections, along with the current section, were performed using VMAT lung SABR plans collapsed to a gantry angle of 0°, and incident on the solid water phantom used for measurements. These collapsed plans were exported from Eclipse and calculated using the validated MC model.

The peripheral dose given by the 10X-FFF treatment was compared to the peripheral doses for 10X and 6X for each plan. The relative peripheral doses for all three energies were also evaluated between the six cases.

3.3.2 Monte Carlo Simulations - Arc Delivery

The final phase of the VMAT Lung SABR study was performed when VMAT capability became available with the MC system. The six cases were recalculated in MC, simulating a true arc delivery (with the gantry continuously rotating around the patient while the beam is on). These arc simulations were performed on the actual patient CT images instead of on the uniform solid water phantom. This allowed for more clinical comparisons to be made between plans. The dose received by normal tissues outside of the treatment axis was evaluated for each plan, and compared between the three energies.

Chapter 4

Results and Discussion: Ion Chamber Measurements and Dose Calculation Algorithm Validation

This chapter presents the results of the first two components of this project, ion chamber measurements and dose calculation algorithm validation, which were described in chapter 3.

4.1 Ion Chamber Measurements

The results of the ion chamber measurements for Static Open fields, Static MLC fields and Dynamic MLC fields are presented below. Additional plots can be found in Appendix A.

4.1.1 Static Open Fields

The ion chamber measurements for Static Open fields (10×10 cm^2 and 5×5 cm^2 fields sizes and measurement depths of 5 cm and 10 cm) are shown on semilog plots in figure 4.1. The dose is plotted relative to the CAX dose for each field size and measurement depth. The 0 cm marker indicates the CAX. The dose was compared in the peripheral region, which was defined as the dose outside of the in-field and penumbral regions.

Figure 4.2 show the ratio of 10X-FFF dose to the flattened 6X and 10X doses. In these four cases, the ratio is always ≤ 1 in the out-of-field region, meaning that 10X-

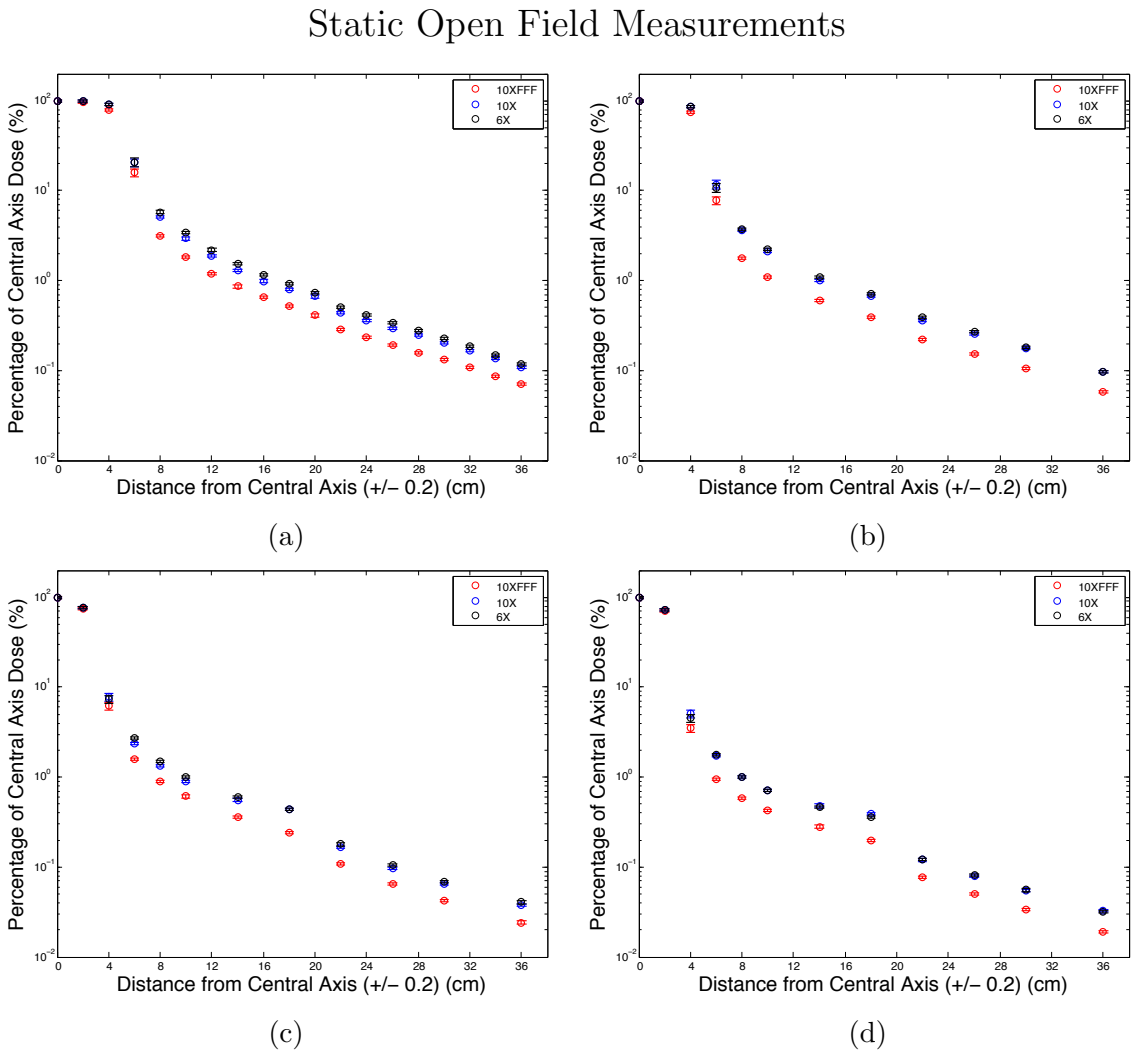

Figure 4.1: Static Open field measurements: a) 10×10 cm^2 field size, measurement depth 10 cm, b) 10×10 cm^2 field size, measurement depth 5 cm, c) 5×5 cm^2 field size, measurement depth 10 cm, d) 5×5 cm^2 field size, measurement depth 5 cm. 10X-FFF is shown in red, while 10X and 6X are shown in blue and black, respectively.

FFF produced a reduced peripheral dose compared to 6X and 10X beams. Outside of the field, the 10X-FFF dose was 30% to 50% lower than the dose for 10X and 6X beams, with an overall average reduction of $42 \pm 4\%$ when compared to 6X, and $38 \pm 5\%$ when compared to 10X.

For all energies and measurement depths, the out-of-field dose falls off roughly exponentially with increasing distance from the field edge (appearing linear on the semi-log plot), and decreases with decreasing field size. These characteristic of dose fall-off outside of the field is expected, and have been shown in the literature [35]. For all fields and measurement depths, 10X-FFF delivered a lower dose in the peripheral region than either 6X or 10X. This was anticipated due to the absence of scatter originating in the flattening filter, as described in section 2.2. Figure 4.2 demonstrates that the FFF/FF ratio is less than 1 for both 10X-FFF/10X and 10X-FFF/6X. The two ratios agree relatively well with each other for measurements performed at a depth of 5 cm, while at a measurement depth of 10 cm the ratio of 10X-FFF to 6X is significantly smaller than that of 10X-FFF to 10X. This indicates that for the same field, the peripheral dose at a depth of 5 cm is similar for 10X and 6X beams, but at a depth of 10 cm, it would be higher for 6X beams. The peripheral dose for 10X-FFF at either depth is shown to be lower than the peripheral doses for 10X and 6X.

The FFF/FF ratio plots demonstrate a similar shape to the MC-calculated FFF/FF plots presented by Kry et. al [11]. Immediately outside of the field in the penumbra region, the FFF/FF ratio is less than 1 and decreasing. It reaches a distinct point at approximately 3 to 4 cm outside of the field where the ratio increases slightly. It reaches another local minimum approximately 12 cm later, after which it remains relatively constant. In general, the peripheral dose region can be separated into three regions based on distance from the treatment field edge, according to the relative importance of different sources contributing to dose in that region. These regions are, (1): the penumbra/head scatter region, (2): The patient scatter region, and (3): the leakage radiation region [21]. The ranges and locations of these regions are dependent on energy, depth and field size, however the leakage radiation is thought to start to be significant in the range of approximately 15-30 cm from the edge of the field [11, 13, 21]. The fluctuations in the shape of the FFF/FF ratio plots could be illustrative of the radiation source dominating the peripheral dose at a given point.

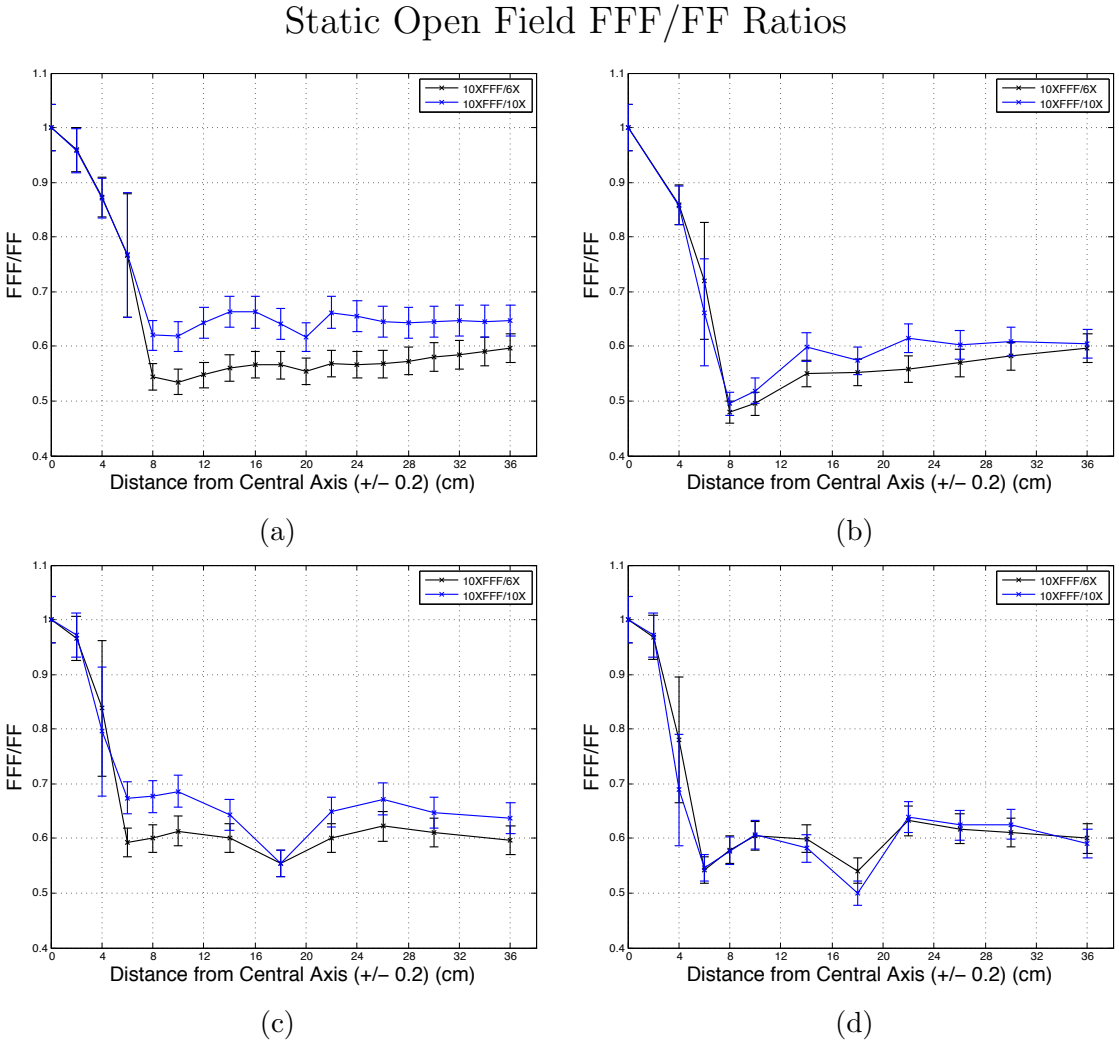

Figure 4.2: FFF vs. FF3 beam ratio for each static open field, a) 10×10 cm^2 field size, measurement depth 10 cm, b) 10×10 cm^2 field size, measurement depth 5 cm, c) 5×5 cm^2 field size, measurement depth 10 cm, d) 5×5 cm^2 field size, measurement depth 5 cm. The ratio of 10X-FFF to 10X and 6X are shown in blue and black, respectively.

In-Plane vs. Cross-Plane

Figure 4.3 shows a comparison between the measured dose for static fields using the In-Plane (IP) geometry and the measured dose for static fields using the Cross-Plane (CP) geometry, for 10X-FFF (plots for other energies can be found in appendix A). For all energies, the measurements agree within 2% inside the field, but start to disagree more outside of the field. In all cases, the CP measurements is lower in dose compared to the IP measurements past 20 cm from the CAX. Across all energies, the difference between CP and IP dose in the peripheral region reaches as much as 40% to 54% of the local dose.

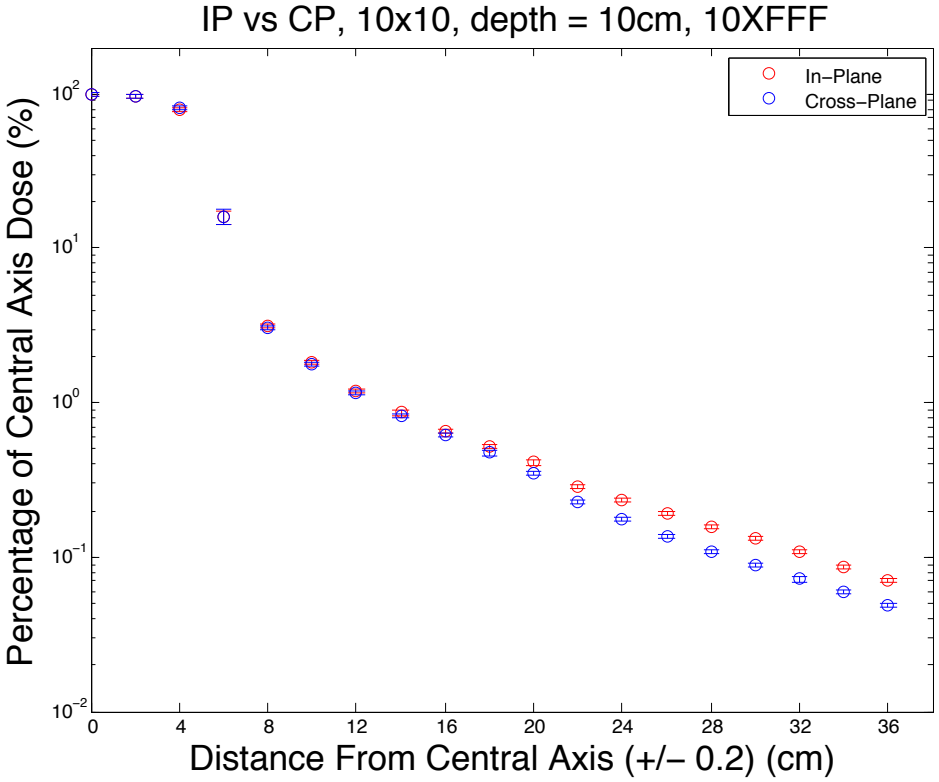

Figure 4.3: In-plane (in red) vs cross-plane (in blue) for 10XFFF (static open, 10x10, depth = 10 cm).

As shown in figure 4.3, the measured peripheral dose is lower outside of the treatment field in the CP direction, as compared to the IP direction. This phenomenon agrees with the published literature [25, 49], explained by the position of the jaws and MLC carriage within the linac head. The upper y-jaws produce a large amount of scatter due to their proximity to the target. The scatter from the y-jaws remains uncollimated in the IP direction due to the positioning of the x-jaws and the MLC

carriage, which move in the x-plane (perpendicular to the y-plane). In the CP direction, the x-jaws and the MLC carriage extend in the x-plane and collimate scatter produced higher in the linac head. This reduces the amount of head scatter delivered to the patient in the x-plane. The difference in peripheral dose between the IP and CP measurements was found to be as high as 54%. Previous work has included recommendations for IMRT treatments to be delivered with the x-plane aligned with the craniocaudal axis of the patient in order to minimize peripheral dose [25], however VMAT plans are generally delivered with a 45° or 315° collimator rotation to minimize the effect MLC inter-leaf leakage. Therefore this minimization of peripheral dose through treatment setup is likely not a practical option for VMAT treatments.

4.1.2 Static MLC Fields

The ion chamber measurements for static MLC fields are presented in this section. The Static MLC field measurements were taken at a depth of 10 cm, for a 6×6 cm^2 field defined by the MLC, while the jaws defined an 8×8 cm^2 field size. Figure 4.4 shows the relative dose vs. distance from the CAX, and the ratio of 10X-FFF dose to 10X and 6X dose vs. distance from the CAX. The reduction in peripheral dose offered by 10X-FFF as compared to 6X is in the range of 30% to 40%, with an average out-of-field reduction of 33 ± 4%. Similarly, 10X-FFF delivers a 3% to 33% lower dose as compared to 10X, with an average reduction of 16 ± 11%.

It is clear from comparison of figures 4.2 and 4.4 that the reduction of peripheral dose by 10X-FFF in the peripheral region is diminished when the MLC are introduced into the field. One explanation for this phenomenon is the effect of shielding by the MLC in the beam. A contributing factor in the reduction of peripheral dose associated with flattening filter free beams is the absence of scatter from the flattening filter, making the head scatter component of peripheral dose significantly less than that of flattened beams. While this advantage still exists when the MLC are utilized within the field, the MLC may shield some of the scatter originating in the flattening filter for 6X and 10X, reducing the magnitude of the difference between flattened and flattening filter free beam peripheral doses. Additionally, the presence of the MLC within the field adds a scatter component to the overall head scatter for each field. The magnitude and location of the increase in peripheral dose caused by the MLC scatter will be different for different energies, and will also contribute to the change in the FFF/FF shape for the Static MLC fields compared to the Static Open fields.

The 10X-FFF/10X and 10X-FFF/6X ratios for Static Open fields shown in figure 4.2 are relatively similar in shape. The two ratios for the Static MLC field maintain this relationship in the distant part of the peripheral region (approximately 20 cm and further from the CAX). However, a few centimetres outside of the field, the two deviate when the 10X-FFF/10X ratio shows a distinct bump, while the 10X-FFF/6X ratio remains relatively flat, between 0.7 and 0.6. The cause for this bump may be the nature of scatter from the MLC and within the patient for different energies, and a similar effect has been observed by others [11, 32]. While high energy scatter is generally more forward peaked, lower energies particles scatter at larger angles. Therefore peripheral dose associated with the 6X beam at this location may be higher due to the increase in lateral scatter originating from the MLC leaves, while the dose contribution from the MLC scatter at this location is more similar for 10X-FFF and 10X fields, due to the forward peaked-scatter for higher energies.

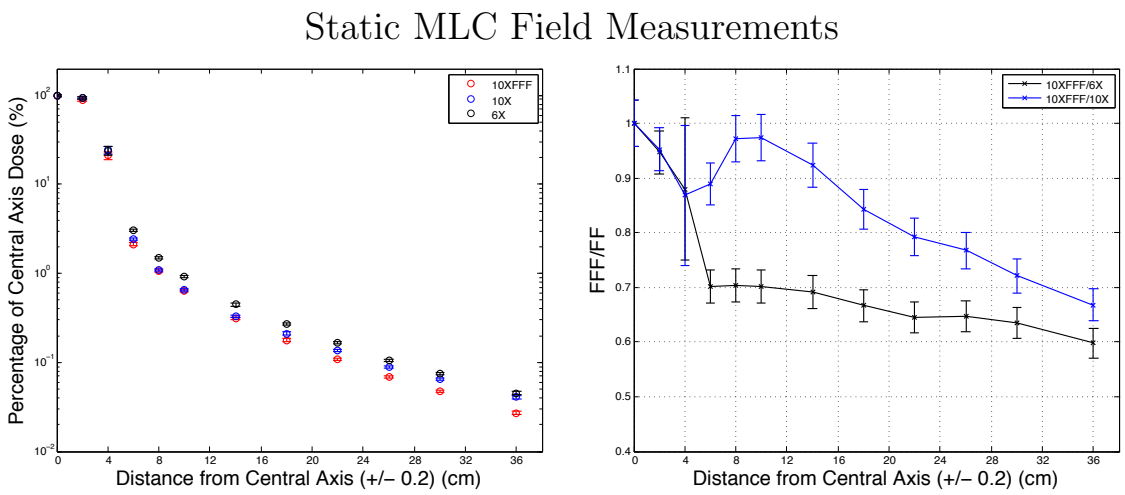

Figure 4.4: a) Static MLC measurements, b) Static MLC FFF vs. FF ratio.

4.1.3 Dynamic MLC Fields

The ion chamber measurements for dynamic MLC fields are presented here. Figure 4.5 a) and b) show the dose measurements at a depth of 5 cm for each energy, and the associated FFF/FF ratio plot. While the FFF/FF ratio remains ≤ 1, outside of the field the reduction ranges from 5% to 15% for the 10X-FFF/10X ratio, and 10% to 20% for the 10X-FFF/6X ratio. The mean values for the out-of-field reduction in dose are $11 \pm 3\%$ and $13 \pm 1\%$ for 10X-FFF/10X and 10X-FFF/6X, respectively.

Figure 4.5 c) and d) show the dose measurements in the solid water phantom with low-density lung inserts at a depth of 10 cm for each energy, and the associated FFF/FF ratio plot. The FFF/FF ratio for the measurements in the solid water with lung phantom is ≤ 1 in the peripheral region, with dose reduction for 10X-FFF as compared to 10X and 6X in the range of 10% to 23% with average reductions of $16 \pm 5\%$ and $19 \pm 3\%$, respectively.

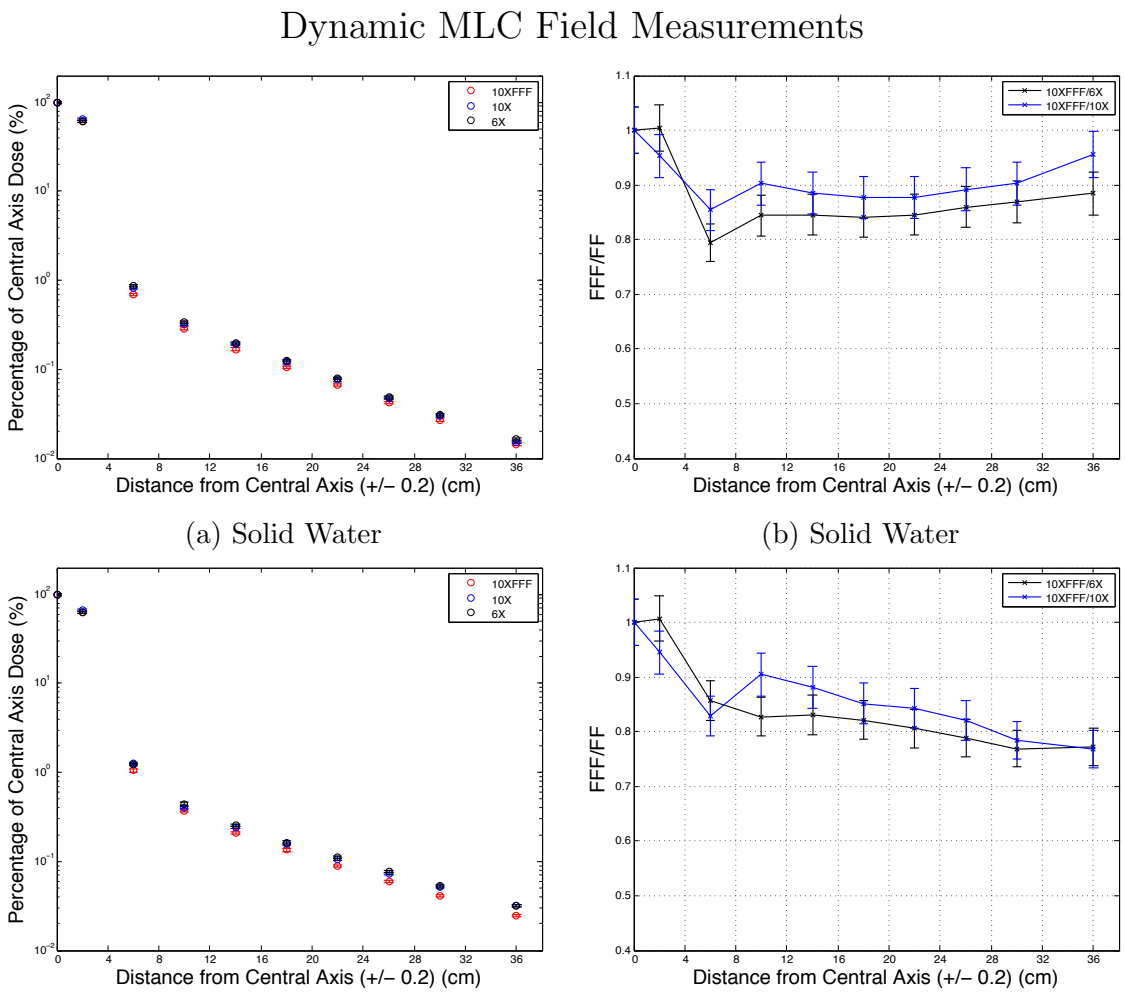

(a) Solid Water

(b) Solid Water

(c) Solid Water with Lung

(d) Solid Water with Lung

Figure 4.5: a) Dynamic MLC measurements, b) Dynamic MLC flattening filter free vs. flattened beam ratio, c) Dynamic MLC measurements, and d) Dynamic MLC flattening filter free vs. flattened beam ratio.

These plots show that further modulation of the field by the dynamic MLC motion during treatment delivery again decreases the reduction in peripheral dose delivered by 10-XFFF as compared to 10X and 6X treatments, as did the addition of static MLC

into the field. The heavily modulated fields mean that peripheral doses measured far outside of the field are very small, and consequently the differences between measured peripheral doses for the three energies become more difficult to distinguish. However, like the Static MLC field FFF/FF ratios presented in figure 4.4, these FFF/FF ratios remain less than 1 in the peripheral region. This indicates that the reduction in peripheral dose offered by 10X-FFF is present and significant for dynamic MLC fields.

The measurements for the solid water phantom with low-density lung inserts are difficult to compare to the measurements performed using the homogeneous solid water phantom, due to the measurements in these two cases being performed at different depths. This was done because the phantom with lung inserts was designed to be a realistic representation of the geometry of a patient's thorax region, and the solid water slice that housed the ion chamber was found at a depth of 10 cm, while the solid water only measurements had already been performed at a depth of 5 cm. However, the low-density measurements appear to be similar to the measurements using the homogeneous solid water phantom, and will be discussed further in section 4.2.

4.2 Validation of Monte Carlo, Acuros XB and AAA Algorithms for Peripheral Dose

The dose delivered by the different types of fields studied in this project was calculated using different dose calculation algorithms, and compared to the ion chamber measurements for those fields. This section presents the results from the validation of different dose calculation algorithms for the peripheral dose region.

4.2.1 Static Open Fields

AAA and Acuros XB

The peripheral doses calculated by AAA and Acuros XB are presented in this section, using the measured ion chamber dose as a comparison. Figure 4.6a shows the AAA predicted peripheral dose for each energy, while figure 4.6b shows the Acuros XB predicted peripheral dose (for a $10 \times 10\,\text{cm}^2$ field size and measurement depth of 10 cm).

Both algorithms predict a dose that rounds off to a low value, close to 0%, at

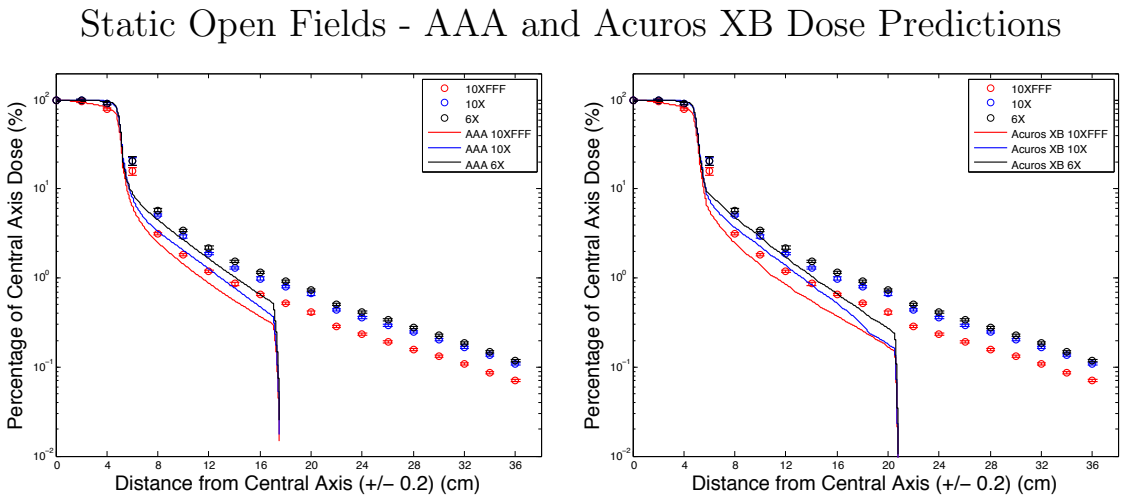

(a) AAA (b) Acuros XB

Figure 4.6: The predicted peripheral dose calculated by AAA and Acuros XB for measurements taken at a depth of 10 cm for a Static Open $10 \times 10\text{cm}^2$ field.

a point approximately 10 cm (AAA) and 15 cm (Acuros XB) from the field edge. Increasing the prescription dose in Eclipse had no effect on this phenomenon. This is a known, and well-documented issue with many treatment planning systems, which are not designed to accurately predict out-of-field doses [37, 50, 25]. Due to this, both AAA and Acuros XB significantly fail to predict the dose far from the treatment field.

However, even in the part of the peripheral region close to the treatment field, the two algorithms fail to calculate a dose that agrees with measurements. Clinically, these algorithms are used for in-field dose calculation, and they have good agreement with measurement in this region. However, due to their lack of success in all regions outside of the field, the validation of these algorithms for peripheral dose prediction was not pursued.

Monte Carlo

The MC-calculated dose predictions are presented here in comparison to the ion chamber measurements. For Static Open fields, two versions of MC were used to calculate dose distributions. "Quick MC" is a simpler version of MC (taking less time to run), while "Advanced MC" is more complex, requiring more computing time. Both are described in section 3.2 of chapter 3. Figure 4.7a shows the Quick MC results for the same $10 \times 10\ \text{cm}^2$ static open field and measurement depth of 10 cm, for all three energies. Similarly, the peripheral dose calculated with Advanced

MC compared with the ion chamber measurements is shown in figure 4.7b. Local percent differences between measurement and MC are shown in these figures. Quick MC accurately predicts dose in the field (less than 5% difference), but the agreement becomes worse in the peripheral region, generally in the range of 30% to 50%. With the exception of one point in the high dose gradient penumbra region, the percent difference between measurements and Advanced MC is generally in the 0% to 20% range, and $\leq 5\%$ in the field.

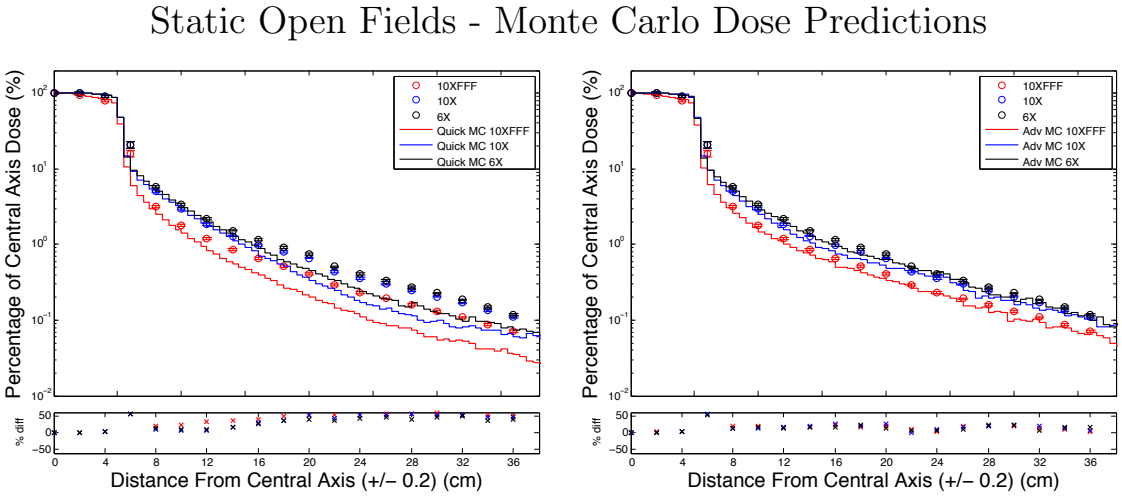

(a) Quick MC (b) Advanced MC

Figure 4.7: MC calculated doses compared to measured doses, for a Static Open $10 \times 10\text{cm}^2$ field and measurement depth of 10 cm.

Quick MC agrees with measurements in the field, with gradually increasing disagreement as distance from the central axis increases. However, they do demonstrate a marked improvement for peripheral dose prediction over both AAA and Acuros XB, where they do not plateau at a value close to 0%. As mentioned in chapter 2, Quick MC uses Phase-Space Collimation jaws which do not model transmission or scatter coming from the jaws, so this discrepancy in the peripheral region is unsurprising.

The dose calculated by Advanced MC (using BEAMnrc and DOSXYZnrc codes) shows a notable improvement over Quick MC, AAA and Acuros XB, in terms of peripheral dose prediction. Although it systematically underestimates the dose in the peripheral region, it is the best predictor out of all dose calculation algorithms tested for the Static Open field case. The fact that MC under-predicts the dose in the peripheral region is not surprising, because the MC system does not model leakage radiation originating from the treatment head [42]. Treatment head leakage

is a significant contributor to peripheral dose, and is the most important component of peripheral dose at distances greater than 15-30 cm from the treatment field edge [11, 13, 21]. We anticipated that MC would under-predict the dose in the peripheral region, especially far from the treatment field, and this could account for the local percent differences of $\leq 20\%$ between measurement and MC.

Figure 4.8 summarizes the peripheral dose prediction accuracy of the four dose calculation algorithms for the 10×10 cm^2 static open field and a measurement depth of 10 cm. The corresponding summary plots for 10X and 6X can be found in Appendix A. Quick MC, AAA and Acuros XB yielded calculation times on the order of minutes, while the calculation time for Advanced MC was on the order of hours for these cases. However, the poor peripheral dose prediction was not worth the more efficient calculation in this case. Due to these results, Advanced MC was the only dose calculation algorithm carried forward in this project as we progress to more complex fields.

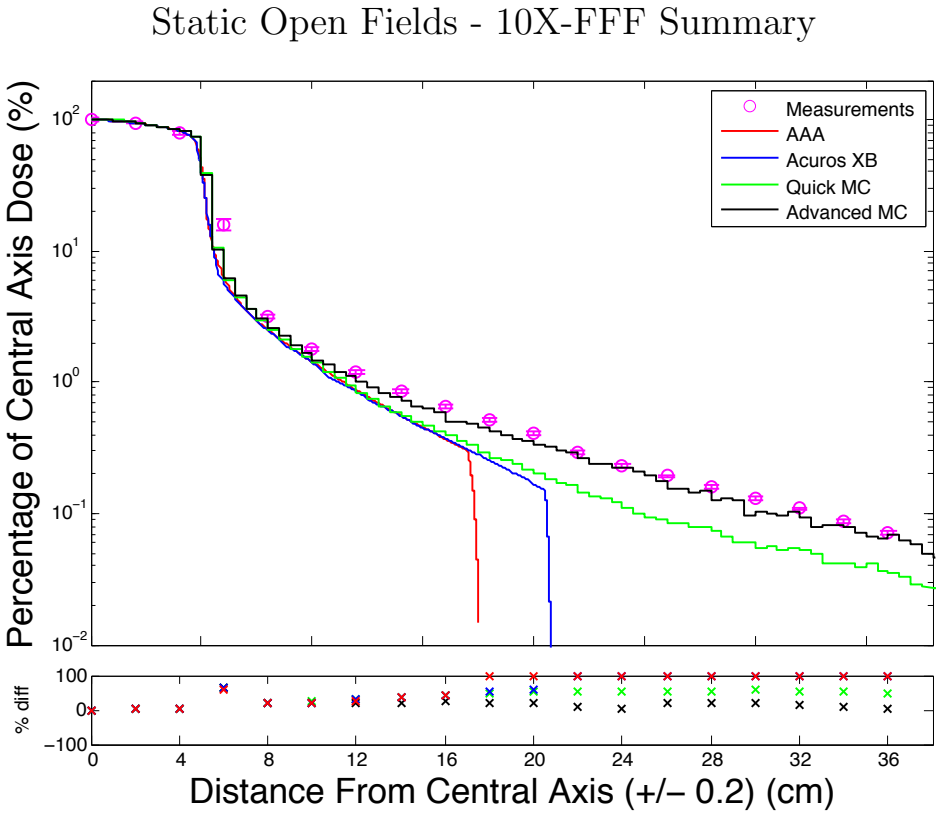

Figure 4.8: Dose calculation algorithm comparison for the 10×10cm^2 field and measurement depth of 10 cm.

4.2.2 Static MLC Fields

Monte Carlo

To evaluate the dose calculation algorithms for peripheral dose prediction for Static MLC fields, the most effective algorithm from the previous section was carried forward, while the algorithms that failed to accurately predict the peripheral dose for the simplest case were excluded. Advanced MC was used for the more complex cases, Static and Dynamic MLC Fields. There are two MLC models used with Advanced MC (VCU DMLC and DYNVMLC), which were evaluated with the use of these fields. The MLC model is not a factor for Static Open fields, since the MLC does not shape or attenuate the beam (and is not used at all in the simulation of these fields).

The dose calculated by Advanced MC using the VCU DMLC model, as well as the ion chamber measurements, are shown in Figure 4.9a. The local percent difference for this comparison is as large as 74%, and generally larger than 20%.

Figure 4.9b shows the dose calculated by Advanced MC using the DYNVMLC model. The dose calculated using Advanced MC with this MLC model demonstrates much better agreement with measurements, with local percent differences generally less than 20%, and as small as 4%, outside of the high dose gradient region.

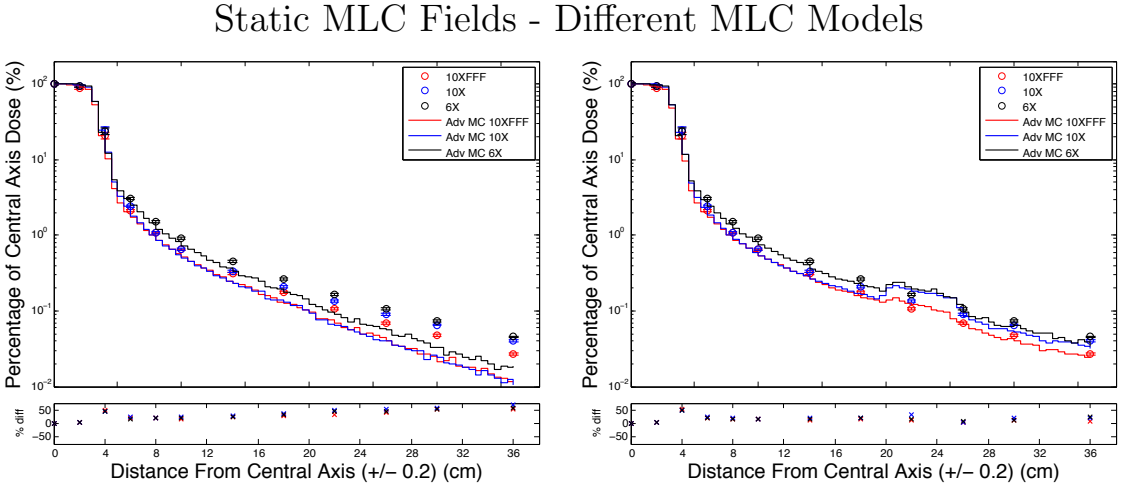

(a) VCU DMLC (b) DYNVMLC

Figure 4.9: Advanced MC dose calculations compared to measurements, using two different MLC models.

The results shown in figure 4.9 indicate that the dose calculated by Advanced MC using VCU DMLC model shows a large disagreement with dose measurement in the

peripheral region. This model uses certain approximations to model scatter from the MLC leaves, which increases calculation efficiency, and is designed for use for in-field calculations [44].

The results using the DYNVMLC model show an improved agreement with measurement in the peripheral region. One notable characteristic of this profile is the "bump" found in the 20-25 cm region. This artifact is thought to be a consequence of the geometry of the MLC model producing scatter during dose calculation. The effect was only observed to be a factor in the in-plane direction, at a collimator rotation of 0°, and was not seen in the cross-plane direction. These results were run several different times to rule out a statistical fluctuation as the cause, but further investigation into the cause was not pursued. Further dose calculations within this project, including the dynamic MLC fields and lung SABR plans, are calculated with collimator angles of 45° or 315° and do not appear to be affected by this phenomenon.

4.2.3 Dynamic MLC Fields

The Advanced MC with DYNVMLC model was used for the remainder of this project, due to its improved agreement with measurements compared to Advanced MC with VCU DMLC. Figure 4.10 shows the comparison between the ion chamber measurements for a dynamic MLC field and the Advanced MC with DYNVMLC calculated dose. The percent difference between measurement and MC remains generally $< 20\%$ for all energies, in the peripheral dose region. For the DYNVMLC predictions in the solid water phantom with low-density lung inserts, the percent differences between measurement and MC is found to be slightly higher, particularly further from the field.

The Advanced MC with DYNVMLC remains suitable for dose calculation in the peripheral region for Dynamic MLC fields. As mentioned in the above sections, due to the absence of treatment head leakage modelling in MC, the under-prediction of dose is expected. The agreement of MC with measurements remains in the 0% - 20% range for the peripheral region.

The results for the Dynamic MLC field in the inhomogeneous phantom remain acceptable, albeit slightly worse than the results for the homogeneous phantom. There could be several factors contributing to this phenomenon. The MC results for low-density materials have been known to be more sensitive to the electron low energy cut-off set for the simulation than higher density media [45], which could cause the

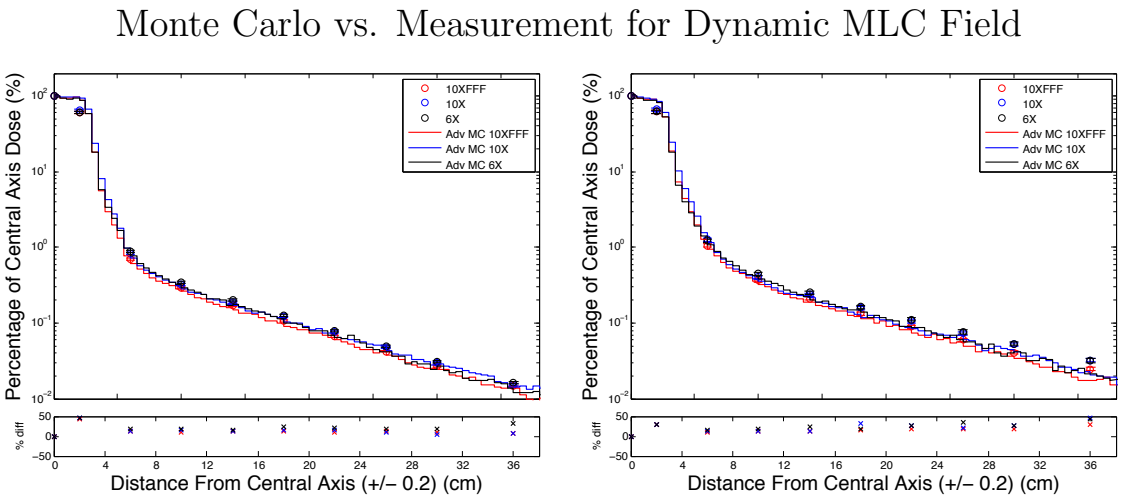

(a) Solid Water (b) Solid Water with Lung Insert

Figure 4.10: The predicted peripheral dose for the Dynamic MLC Field calculated by Advanced MC (DYNVMLC), using different phantom densities.

slight increase in the local percent differences for these results. Additionally, the absence of the treatment head leakage component of the MC-calculated dose would be more significant in the low-density material, because more leakage radiation will reach the measurement point. The leakage radiation will cause the ion chamber measurements to increase, creating a larger difference between measurements and MC in the inhomogeneous phantom.

4.3 Summary

The ion chamber measurements of peripheral dose, and dose calculation algorithm validation results were presented and discussed in this chapter. Ion chamber peripheral dose measurements for static open fields, static MLC fields and dynamic MLC fields were presented at two different field sizes and measurement depths. For all simple and complex fields, the 10X-FFF measurements of peripheral dose were lower than either 6X or 10X measurements, demonstrating the reduction in out-of-field dose.

AAA, Acuros XB and MC (Quick MC and Advanced MC) were investigated for use for peripheral dose calculation. AAA and Acuros XB were found to under predict the dose (by as much as 100%) in the peripheral region. The Advanced MC using DYNVMLC model was found to be the best predictor of peripheral dose in this

validation, and was carried forward for use in the Lung SABR study.

Chapter 5

Results and Discussion: VMAT Lung SABR Study

This chapter presents the results of the third component of this project, the Lung SABR study, which was described in chapter 3.

5.1 Lung SABR Study

The validated MC model, Advanced MC using DYNVMLC, was used to calculate the dose for six representative SABR cases. Three plans were created for each case, one plan for each 6X, 10X and 10X-FFF. The plans were calculated first using a static gantry delivery in the solid water phantom. Then, they were calculated in their respective patient CT images, with a simulated arc delivery. The results are shown in the following sections. Additional plots can be found in Appendix B.

5.1.1 Monte Carlo Simulations - Static Gantry Delivery

The dose distributions for each plan was calculated in MC. Profiles were taken in the in-plane direction in the resulting dose distributions from the CAX to 36 cm from the CAX, similar to the MC dose profiles presented in chapter 4 as a part of the dose calculation algorithm validation for peripheral dose. The profiles were taken for each plan at depths of 5 cm and 10 cm in the solid water phantom. Figure 5.1 shows the dose profiles at a depth of 10 cm for the six cases for the 10X-FFF plans. The dose profiles for the 10X and 6X plans are shown in the appendix, as well as the analogous dose profiles for all three energies at a depth of 5cm in the solid water phantom.

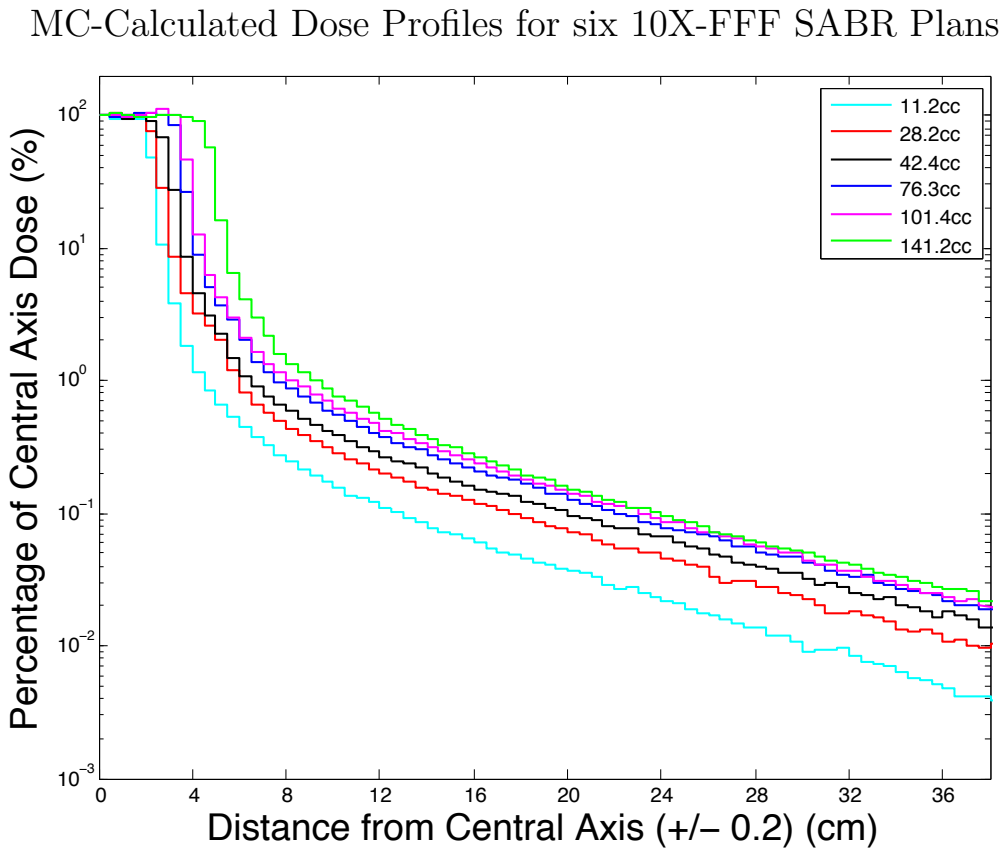

Figure 5.1: Relative dose at a depth of 10 cm as a function of distance from the CAX in the Superior-Inferior direction, for six cases, according to PTV volume.

The results shown in figures 5.1 indicate that the dose in the peripheral region decreases in a consistent manner as the distance from the CAX increases, and increases overall with increasing field size (larger PTV volumes require, in general, larger MLC and secondary collimator apertures). This observation is in agreement with the results shown by Taylor et. al. [25]. Figure 5.1 shows profiles calculated using the same energy (10X-FFF) and at the same depth, therefore the effect of field size on peripheral dose is caused by changes in the primary fluence between fields [25]. Peripheral dose depends on the primary fluence because primary fluence affects the scattered photon fluence reaching the peripheral region. Scattered photons deliver dose to peripheral structures according to their energy, fluence, and the energy absorption coefficients of the medium at that location. It has been shown that the increase in out-of-field dose is approximately proportional to the side-length increase of the field [25].

These MC-calculated dose profiles were used to calculate a flattening filter free vs flattened beam ratio (FFF/FF) for each case (associated with a particular PTV

volume). Figure 5.2 shows the ratio of the 10X-FFF dose profile compared to the 6X dose profile (10X-FFF/6X ratio) for all six cases, at a depth of 10 cm in the solid water phantom. Similarly, figure 5.3 shows the 10X-FFF/10X ratio for all six cases at a depth of 10 cm. As well, the analogous plots are shown for a depth of 5 cm in the solid water phantom in figures B.4 and B.5, found in Appendix B.

Figures 5.2 and 5.3 show the FFF/FF dose ratios for each of the six cases, designated by their PTV volumes. The 10X-FFF/6X ratio falls predominantly below 1 outside of the field for all cases, though the uncertainty in the distant peripheral region is very high for some. The 10X-FFF/10X ratio appears to be predominantly below 1 for the majority of cases, but less so than the 10X-FFF/6X ratio, falling above 1 at some point along the profile for most cases.

To summarize the peripheral dose reduction seen in these profiles, the mean FFF/FF value for each profile was calculated over the peripheral region. These results are shown in table 5.1. The ratios for 10X-FFF compared to 6X were found in the range of 0.79 to 0.93, and the ratios of 10X-FFF compared to 10X were found in the range of 0.83 to 0.93. These ratios translate into reductions in peripheral dose of 7 to 21% and 7 to 17% for 10X-FFF compared to 6X and 10X for these cases.

Mean FFF/FF Ratios

PTV	**FFF/6X**		**FFF/10X**	
Volume (cc)	**depth 10 cm**	**depth 5 cm**	**depth 10 cm**	**depth5 cm**
11.2	0.80 ±0.01	0.86 ±0.01	0.92 ±0.02	0.89 ±0.01
28.2	0.89 ±0.02	0.93 ±0.03	0.93 ±0.02	0.89 ±0.02
42.4	0.87 ±0.01	0.91 ±0.02	0.87 ±0.01	0.83 ±0.02
76.3	0.80 ±0.02	0.85 ±0.04	0.93 ±0.02	0.88 ±0.03
101.4	0.82 ±0.01	0.85 ±0.02	0.93 ±0.01	0.90 ±0.02
141.2	0.79 ±0.02	0.81 ±0.02	0.93 ±0.01	0.87 ±0.02

Table 5.1: Mean FFF/FF for each case.

These results would benefit from re-calculation resulting in lower statistical uncertainties. The MC system is not designed for out-of-field dose calculation, and the selection of the desired level of uncertainty specifies the uncertainty of the in-field results. Even a selection of in-field uncertainties of 0.1-0.5% gives local uncertainties on the order of 5-20% in the peripheral region. It is possible to continue to decrease

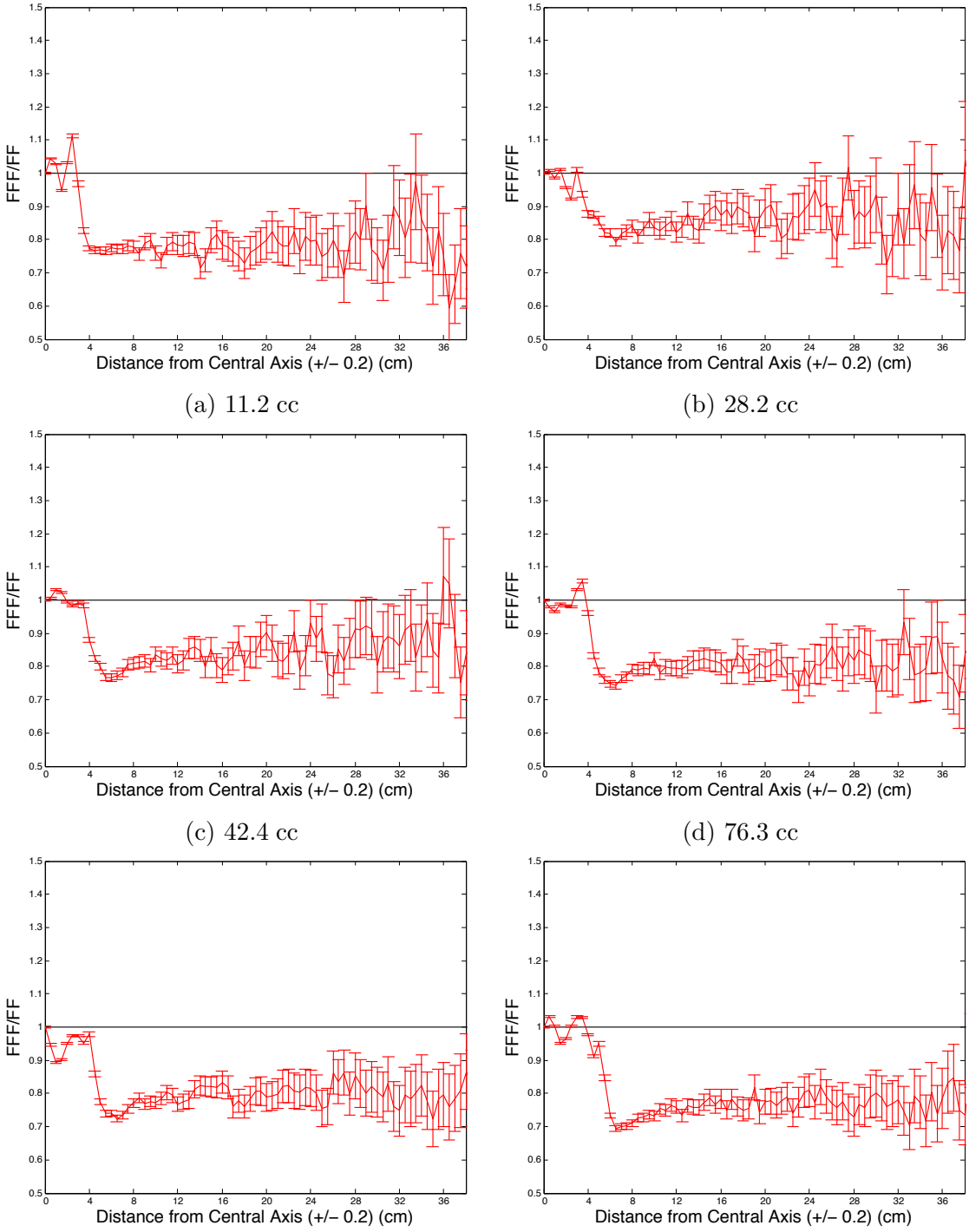

(a) 11.2 cc

(b) 28.2 cc

(c) 42.4 cc

(d) 76.3 cc

(e) 101.4 cc

(f) 141.2 cc

Figure 5.2: 10X-FFF/6X ratio at a depth of 10 cm in the solid water phantom, for each of the six cases.

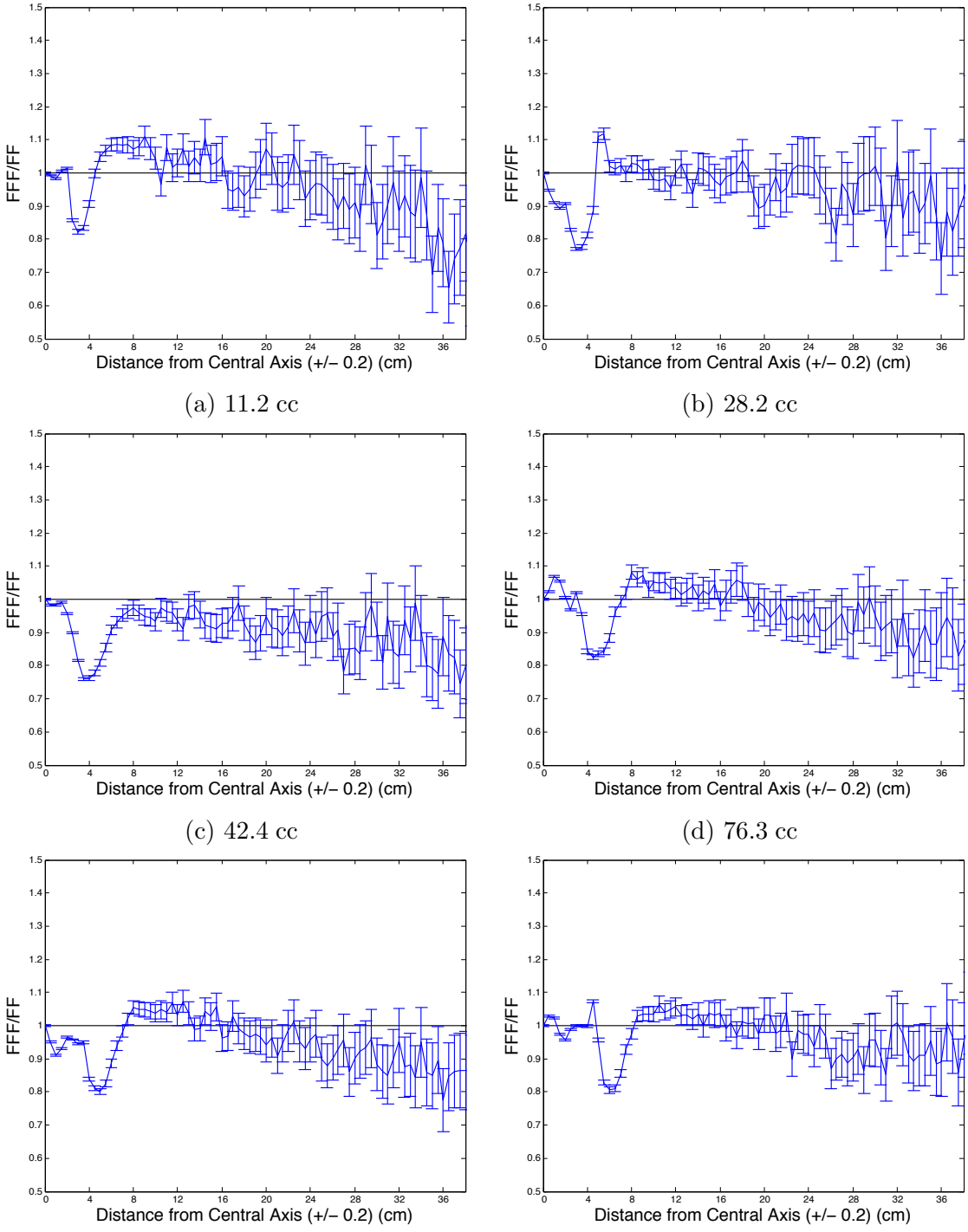

(a) 11.2 cc

(b) 28.2 cc

(c) 42.4 cc

(d) 76.3 cc

(e) 101.4 cc

(f) 141.2 cc

Figure 5.3: 10X-FFF/10X ratio at a depth of 10 cm in the solid water phantom, for each of the six cases.

the level of uncertainty in-field to achieve lower out-of-field statistical uncertainties, but this will also increase computation time. The plans associated with the results presented took several (> 5) hours to complete the calculation. The statistical uncertainty of the results are, in general, proportional to $1/\sqrt{N}$, where N is the number of particles reaching a given point [48]. Therefore, to decrease the statistical uncertainty by a factor of 10, the number of particles in the simulation must be increased by a factor of 100, proportionately increasing calculation time. Increasing the size of the dose grid would help to decrease the statistical uncertainty, because more particles would be included in one voxel. More efficient methods of reducing the statistical uncertainties in the peripheral region while maintaining a manageable calculation time exist, but are outside the scope of this project.

The effect of high uncertainties is seen more prominently for smaller PTV volumes (and field sizes). This is caused by the lower out-of-field photon fluence for these plans. Smaller field sizes require fewer particles overall, so fewer particles reach a point at a given distance from the CAX than for a larger field.

Finally, as previously mentioned in chapter 2, the MC calculation does not include the treatment head leakage component. FFF beams require less target current per MU [32]. Due to this increase in delivery efficiency, the treatment head leakage component is reduced for the 10X-FFF beam, and the difference between the MC-calculated peripheral doses for 10X-FFF fields and 10X and 6X fields would be larger than the MC results indicate.

5.1.2 Monte Carlo Simulations - Arc Delivery

The dose distributions for each plan was calculated in its respective patient anatomy, using the patient CT scans. Dose calculation in patient anatomy makes it possible to give a more practical perspective on the advantages of lowering peripheral dose for a real patient. To assess the dose reduction effect in the real patient scenario, the doses delivered to the body structure in the peripheral region are examined in this section.

The use of arc deliveries to analyze peripheral dose presents the unique challenge of decisively defining peripheral dose. For static gantry angles, peripheral dose includes all dose to tissues located outside of the primary radiation field. Even if MLC modulation exists for a static gantry angle field, the peripheral dose can still be considered any dose outside of the field (or, the closely related PTV) for the plan. However, the classification of peripheral dose is less clear for the case of an arc deliv-

ery, where the gantry angle is non-static. Tissue at a given point along the plane of the rotating treatment field (for full-arc treatments), is included in the primary beam for at least a fraction of the treatment, so the "out-of-field" label does not necessarily apply to these regions. The truly out-of-field regions of the patient anatomy would be those tissues through which the primary beam does not travel. These tissues are located outside of the beam's eye for the entire treatment, and receive dose solely from scattered radiation.

Ten Percent Dose Geometry

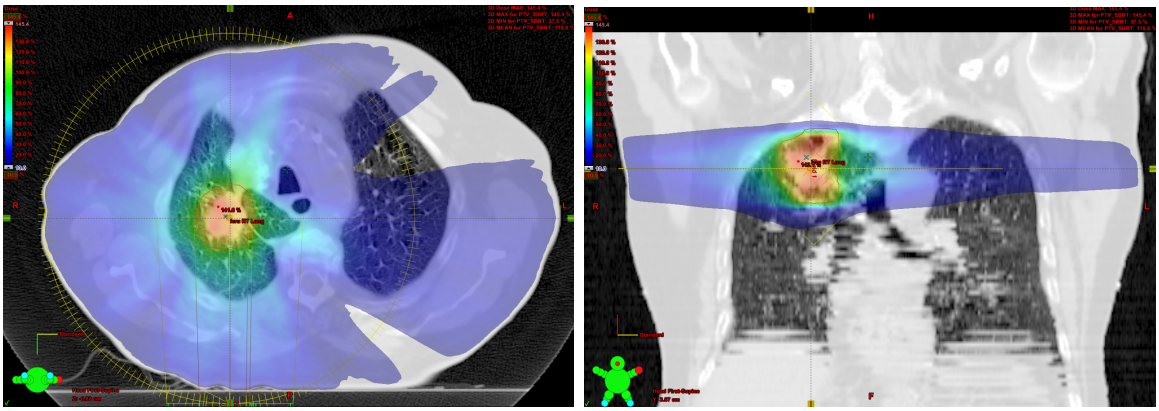

(a) Axial View (b) Coronal View

Figure 5.4: The $\geq 10\%$ dose distribution (shown as a colourwash) for one Lung SABR plan.

The ion chamber measurements shown in chapter 4 indicate that in the peripheral dose region, the dose is generally $\leq 10\%$ of the central axis dose. Figure 5.4 shows the 10% and greater dose distribution for one of the lung SABR plans. This dose distribution generally corresponds with the aforementioned region which excludes tissues that fall within the primary beam at some point during radiation delivery.

The $\geq 10\%$ dose region is contained within a limited number of axial CT slices in the Superior - Inferior direction, and does not extend more than a few centimetres. In order to create a structure that would include only peripheral dose, these axial slices were removed from the unaltered "Body" structure, and the peripheral region was taken as the remaining CT slices through which the primary beam does not travel. This method of defining peripheral dose is specific to the coplanar VMAT technique used in these treatments, and may not be applicable for the general lung SABR case. To ensure consistency, the limits of the section of slices to be removed from the original body structure was taken as the PTV at isocentre plus a margin

of 2 cm. This was found to contain the $\geq 10\%$ dose distribution for all cases. The "Peripheral Body" structure, as shown in figure 5.5 was used to calculate the mean dose received by the body, outside of the primary beam.

Peripheral Body Structure

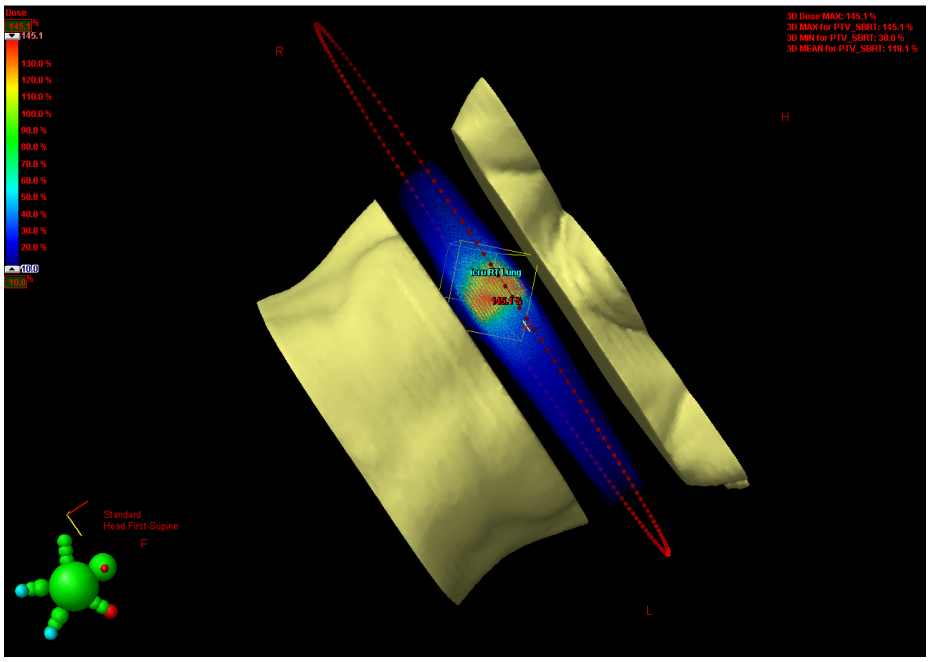

Figure 5.5: The peripheral body structure was created for each case. Here, it is shown for one plan in relation to the 10% dose distribution.

The mean does for the peripheral body structure was taken for each plan, and is shown for each case in figure 5.6. Each PTV volume corresponds to one case, with three (6X, 10X and 10X-FFF) plans. Note that the spacing between sets of bars on this graph does not correspond to the differences in PTV volume between cases. The dose in this figure is displayed as relative dose, where the prescription dose for the whole (4 fraction) lung SABR treatment is 4800 cGy. Therefore, the mean peripheral doses calculated for these cases range from approximately 10 cGy to 43 cGy.

Figure 5.6 shows that, for each case presented in this study, the 10X-FFF plan delivered the lowest mean peripheral dose to the body than the plans using 6X and 10X. However, due to large statistical uncertainties the 10X-FFF and 10X doses are indistinguishable for all cases, and the 10X-FFF and 6X doses are indistinguishable for the two smallest PTV volumes.

Certain other observations can be made from the data presented in Figure 5.6. In general, peripheral dose tends to increase with increasing PTV volume or field size.

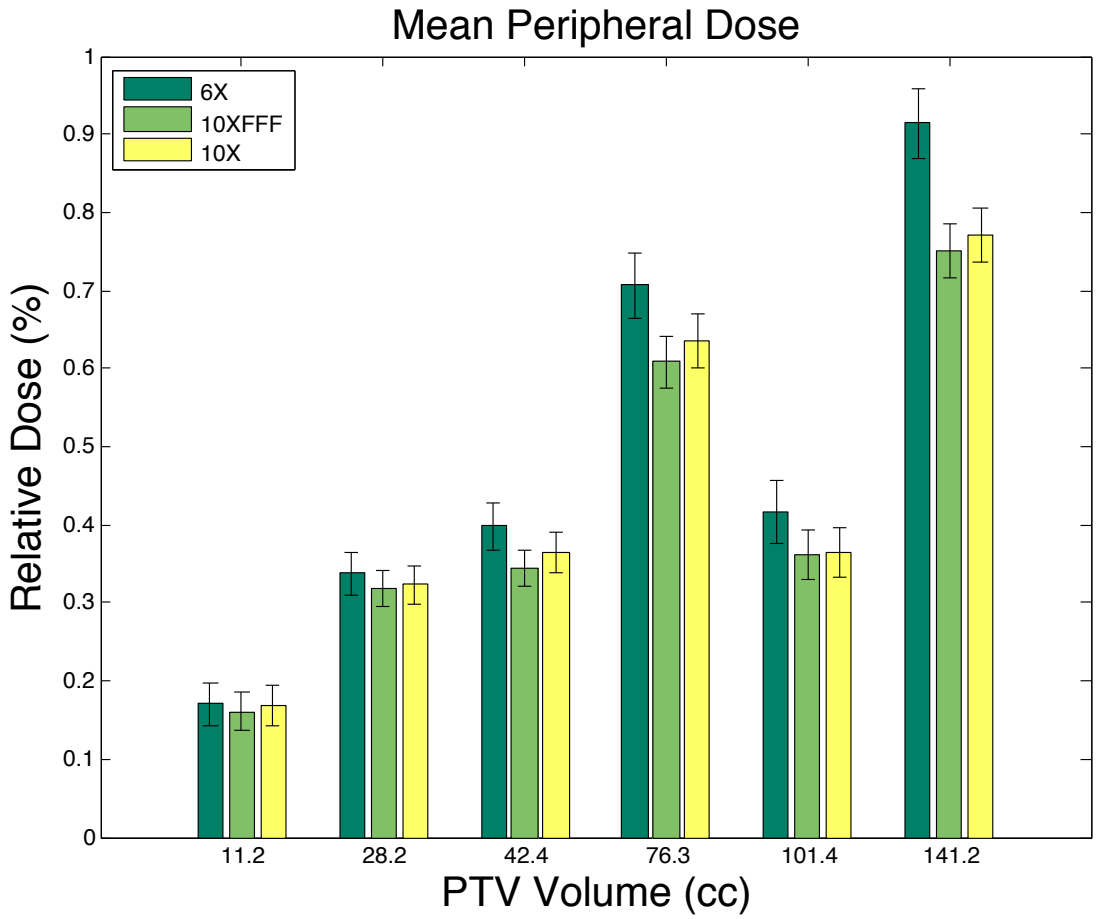

Figure 5.6: Mean dose to the peripheral body structure for each plan and PTV volume.

This is consistent with results presented in the previous section and chapter, and with the published literature [25]. It also appears that the peripheral dose reduction may increase with PTV volume, though determining this with certainty would require a larger sample size.

The mean peripheral dose results are summarized in figure 5.7, which shows the ratios of mean doses for 10X-FFF compared to 6X and 10X, similar to the FFF/FF ratios previously shown in section 5.1.1 and chapter 4. The mean peripheral dose reductions for 10X-FFF vs 6X and 10X-FFF vs 10X were found to be approximately 12% and 3%, respectively. Again, 10X-FFF offers a more distinct advantage over 6X than over 10X. However, further conclusions would require an increase in the sample size of the study, to include more lung SABR cases, and to re-run the calculations using more particles to achieve a lower statistical uncertainty. The uncertainties

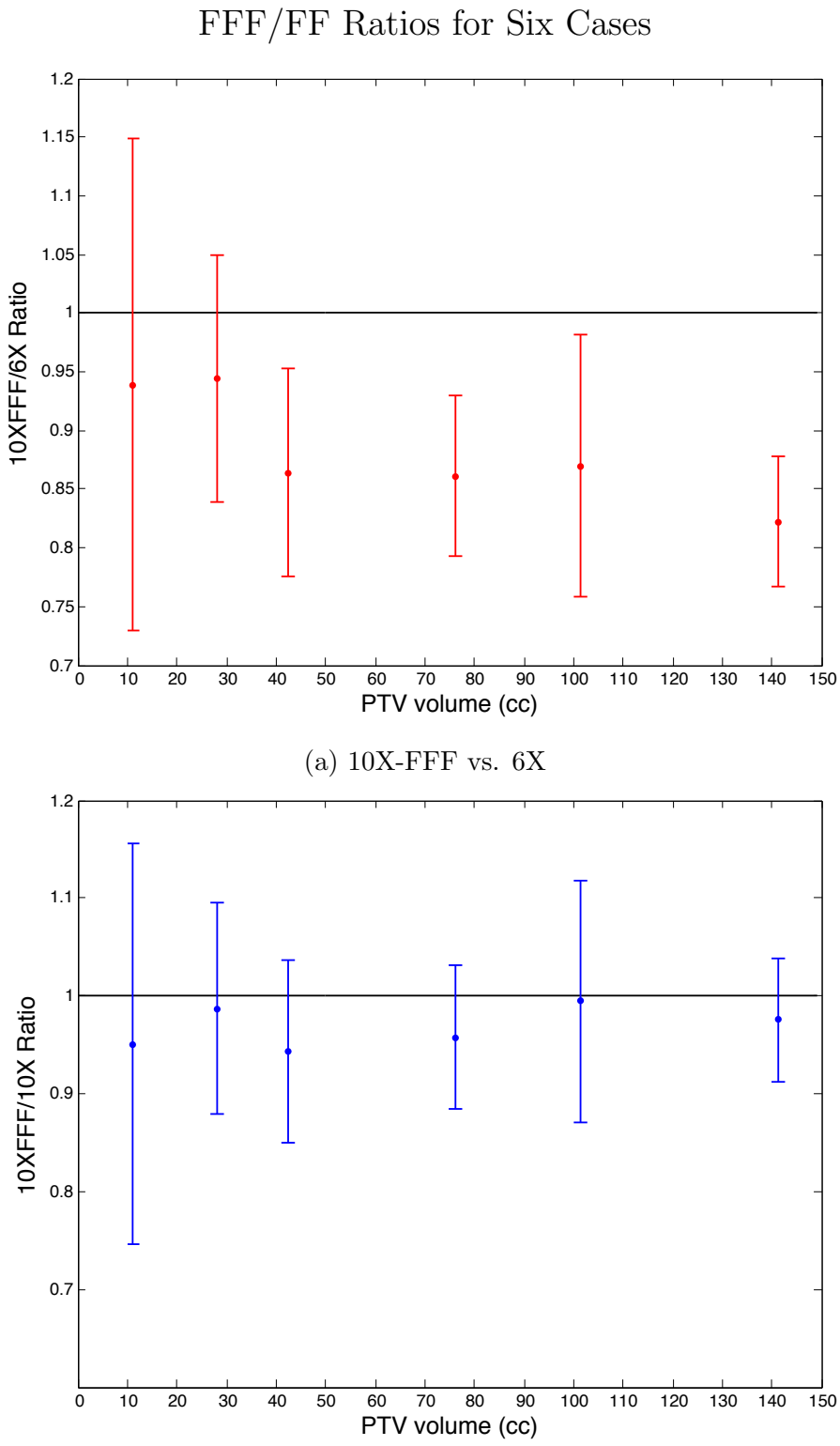

(a) 10X-FFF vs. 6X

(b) 10X-FFF vs. 10X

Figure 5.7: FFF/FF ratios for the mean peripheral doses shown in figure 5.6.

associated with the MC-calculated peripheral doses shown here are the results of the in-field uncertainty selection of 0.5%, as described in section 5.1.1

In interpreting these results, it is important to remember that radiation treatment head leakage is not modelled in MC, and not included in these results. Figure 5.7 shows the mean doses for each case, where the mean doses fall within the range of 0.2-0.9% of the prescription dose. Traditionally, the radiation treatment head leakage component is estimated as 0.1% of the primary beam (in-field) [22], and some studies suggest it may be higher for highly modulated fields [51]. Therefore, the peripheral dose, which is dominated by the treatment head leakage component in the region 15-30 cm or more from the isocentre, would be approximately 0.1% larger for the 6X and 10X plans. Since the body structure largely encompasses those regions, the mean body peripheral dose for 6X and 10X would increase with the addition of the treatment head leakage dose. Meanwhile, the 10X-FFF plans would experience a smaller increase in the calculated dose, due to the decrease in the treatment head leakage component for FFF beams (by a factor of about 4), and the maintenance of a relatively constant number of MU's for these plans between energies.

The restriction in the number of MU's for plans of different energy was done in order to compare the peripheral dose for the same number of MU delivered. Clinically, MU's would not be restricted, so the relative number of MU's between energies should be considered. The relative number of MU's for 10X-FFF and 6X VMAT lung SABR plans has been shown to be in the range of 0.93 to 1.25, systematically increasing with increasing PTV volume [10]. The increase in the number of MU's required for treatment of larger PTV volumes with FFF beams is due to the intensity drop off axis for FFF beams. While the dose to healthy tissues was not shown to follow the same trend as relative number of MU's [10], the reduction in treatment head leakage for FFF beams may be reduced in clinical cases where a large PTV is being targeted.

Another factor affecting these results are the CT images themselves. Radiation therapy planning CT scans do not include a patient's entire body; rather, they are restricted to the region being treated with radiation therapy [21]. To evaluate the peripheral dose received by all tissues outside of the radiation treatment field plane, we would require the entire body image for the MC calculation. Considering the entire body would eliminate artificially low peripheral doses caused truncated CT images. For instance, if the PTV is located at the apex of the lung, and the CT image extends superiorly only 5-10 cm to avoid imaging the entire head, the total peripheral dose for the body would be missing the dose deposited in the head and

neck region by scatter coming from the nearby field. For the same case, if the PTV was located centrally within the lung, more of the peripheral dose would be deposited within the CT volume that exists. This would cause discrepancies in the peripheral dose evaluated, unless a standard was devised for this type of analysis. One solution would be to use whole-body anatomical patient models for this type of study, as discussed by Xu et. al. [15].

It is useful to put the observed reduction in peripheral dose in the context of secondary cancer prevention. Cancer induction is a stochastic process, meaning that there is no dose threshold that guarantees a secondary cancer will develop. This is in contrast to deterministic effects, which are seen after a certain organ receives a minimum dose (e.g., cataract formation or sterility). In terms of a stochastic process, any increase in dose will increase the overall risk of cancer development. Peripheral dose seen in this study is generally found in the range of 0.1% to 3% of the prescription dose, which would be in the range of 0.05 Gy to 1.5 Gy for a prescription dose of 50 Gy. 10X-FFF plans showed a mean reduction in peripheral dose when compared to 6X of approximately 12%. For a the above peripheral dose range, a 12% reduction would reduce the absolute peripheral dose by 60 mGy to 180 mGy. In contrast, natural background radiation is generally 2 mSv/yr (1 Sv = 1 Gy). In terms of radiological protection, the increase in cancer risk for the general population is estimated as 5.5% per Sv [52]. According to this number, a decrease in peripheral dose by 60 mGy to 180 mGy would decrease cancer risks otherwise associated with VMAT lung SABR by 0.3% to 1%. While small, this reduction in cancer risk may be an important consideration for some radiation therapy treatments.

The standard energy for current lung SABR treatments at the BC Cancer Agency is 6X. 10X was included in this study for completeness. The results indicate that there is a reduction in peripheral dose for some 10X-FFF plans as compared to 6X plans, though including more plans in this study would strengthen this finding. The results remain inconclusive on a potential reduction between 10X-FFF and 10X plans, but this is the less important finding since 10X is not used for VMAT lung SABR treatments. While the focus of this project was to evaluate the peripheral doses associated with VMAT lung SABR treatments using 10X-FFF, 6X and 10X, the major advantage of FFF beams for this type of treatment lies in the reduction of treatment time. A reduction in peripheral dose would be an additional benefit offered by FFF beams.

5.1.3 Summary

The results of the lung SABR study were presented and discussed in this chapter. Six VMAT lung SABR cases were planned with each 6X, 10X and 10X-FFF, and each plan was calculated using MC.

Section 5.1.1 included the results from the MC simulations of the static gantry delivery in the solid water phantom. Profiles were taken in the in-plane direction for each plan at two depths. The profiles are shown in the figures as FFF/FF ratios for each plan, and the mean values for each profile are shown in table 5.1. Reductions in peripheral dose for 10X-FFF were found in the range of 7 to 21% and 7 to 17% compared to 6X and 10X, respectively.

The results and discussion for the MC simulations of the arc delivery lung SABR plans in the patient CT's are shown in section 5.1.2. Figure 5.6 shows the mean dose delivered to the peripheral part of the body for each case. It was found that 10X-FFF showed a reduced peripheral dose as compared to 6X for four of six cases, but no significant reduction was shown when compared to 10X.

Chapter 6

Conclusions

The peripheral dose associated with VMAT lung SABR treatments was investigated for three energies through measurement and simulation. The results of this investigation have been presented in this thesis, as well as a discussion of their implications.

Ion chamber measurements of peripheral dose were performed for fields of increasing complexity at different depths, energies and orientations. Measurements of peripheral dose for open, static MLC and dynamic MLC fields for 6X, 10X and 10X-FFF showed that the peripheral dose associated with 10X-FFF fields is the lowest of the three energies. The measurements showed that 10X-FFF offered peripheral dose reductions compared to flattened beams in the range of 30% to 50%, 3% to 40% and 5% to 20% for static open, static MLC and dynamic MLC fields, respectively. Measurements of cross-plane profiles compared to in-plane profiles were lower in the cross-plane direction, but this is not expected to be relevant in VMAT treatments.

The above measurements were compared to AAA, Acuros XB and MC calculated doses for validation of the different algorithms for peripheral dose prediction. AAA and Acuros XB algorithms (used in Eclipse TPS, version 11) were found to significantly under predict the out-of-field dose, and were not carried forward in the validation. Several iterations of Monte Carlo simulations using different models for various treatment head components were analyzed. Advanced MC (all EGSnrc - based) using the DYNVMLC model was found to be the most accurate predictor of peripheral dose of all algorithms assessed in this project. Local percent differences between measurement and MC of $\leq 20\%$ were observed for static open, static MLC and dynamic MLC fields. The absence of the treatment head leakage component in the MC results was discussed as one factor contributing to this discrepancy.

The Advanced MC model was used to calculated the dose for six VMAT lung

SABR treatment cases in both solid water phantoms, and patient CT images. In the solid water phantom, profiles of the peripheral dose at depths of 5 cm and 10 cm indicated that the peripheral dose increases with increasing fields sizes. Peripheral dose reductions were found in the range of 7 to 21% for 10X-FFF compared to 6X, and 7 to 17% compared to 10X.

For dose calculated with arc delivery in the patient CT images, the 10X-FFF plans demonstrated a statistically significant reduction in peripheral dose for four of six cases when compared to 6X. The 10X-FFF plans did not demonstrated a statistically significant reduction in peripheral dose when compared to the 10X plans. Overall, the 10X-FFF plans showed a more distinct advantage in terms of peripheral dose reduction when compared to the 6X plans than when compared to the 10X plans.

Future work includes MC simulations that include the treatment head leakage component of peripheral dose (if possible). Ideally, the MC model should be geared towards peripheral dose calculation, and more efficient ways of simulating out-of-field dose and reducing statistical uncertainty in the peripheral region should be explored. Using MC, the existing plans could be recalculated, specifying a lower statistical uncertainty. The use of whole body phantom models as discussed in chapter 5, would reduce the bias introduced by the location of the PTV in relation to the volume of the acquired CT image. Additional plans should be added to the study to obtain a better picture of the peripheral dose reduction offered by 10X-FFF for the generalized VMAT lung SABR case. Peripheral dose for VMAT lung SABR plans where the number of MU's is not restricted would increase the clinical relevance of these results.

The results presented in this thesis indicate that the majority of VMAT lung SABR plans delivered with 10X-FFF show a reduction in peripheral dose over those plans delivered using 6X. 10X-FFF has been shown by several groups to deliver a dosimetrically equivalent in-field dose distribution to 6X, and 10X-FFF plans have been shown to deliver treatments in significantly shorter treatment times. For these reasons, 10X-FFF is becoming the new standard treatment energy for VMAT lung SABR treatments at the BC Cancer Agency. The reduction in treatment time remains the most significant gain in using FFF beams for high-dose deliveries. The peripheral dose reduction for VMAT lung SABR demonstrated in this thesis adds another advantage of 10X-FFF over 6X for this type of treatment.

Appendix A

Additional Information

Additional figures from chapter 4 are found in this appendix.

A.1 Ion Chamber Measurements

IP vs CP

The In-Plane vs Cross-Plane measurements for the 10 × 10 cm^3 field size at a measurement depth of 10 cm for 10X-FFF was displayed in chapter 4, figure 4.3. Figure A.1 shows the analogous plots for 10X and 6X.

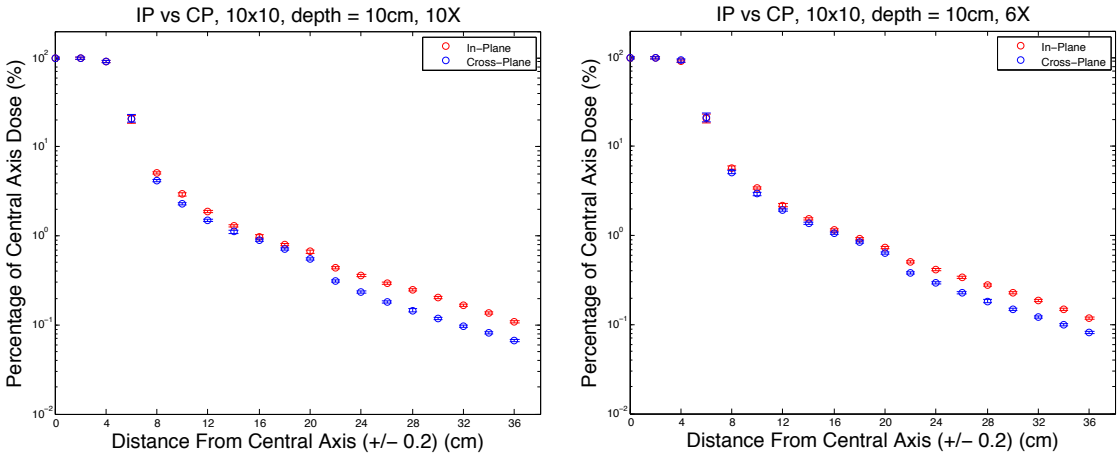

(a) 10X (b) 6X

Figure A.1: IP vs CP for 10X and 6X (static open, 10x10, depth = 10 cm)

A.2 Validation of Monte Carlo, Acuros XB and AAA Algorithms for Peripheral Dose

A.2.1 Static Open Fields

Figure 4.8 shows a summary of the different dose calculation algorithms and measurements using 10X-FFF for the static open field case at a depth of 10 cm. Figure A.3 show the analogous plots for energies of 6X and 10X, and figure A.3 shows the summary plots for all energies at a depth of 5 cm.

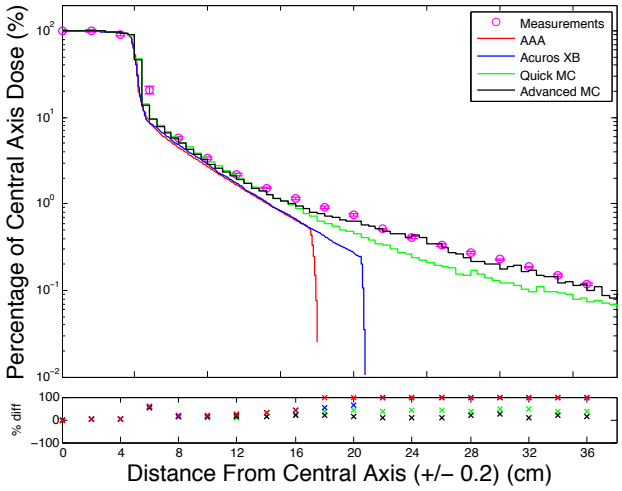

(a) 6X, depth of 10 cm

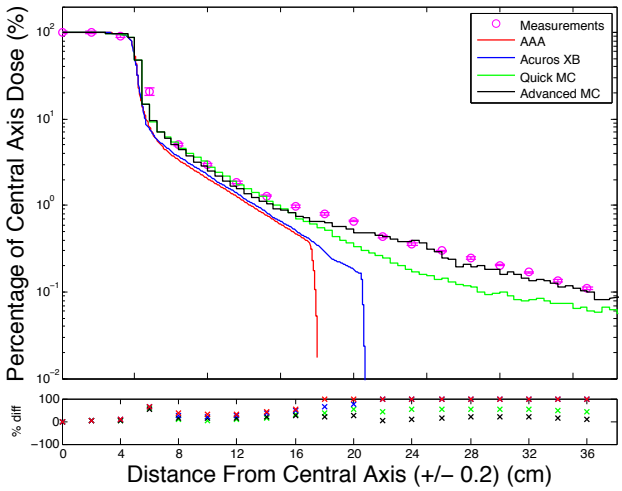

(b) 10X, depth of 10 cm

Figure A.2: Static open field dose calculation algorithm comparison for 6X and 10X.

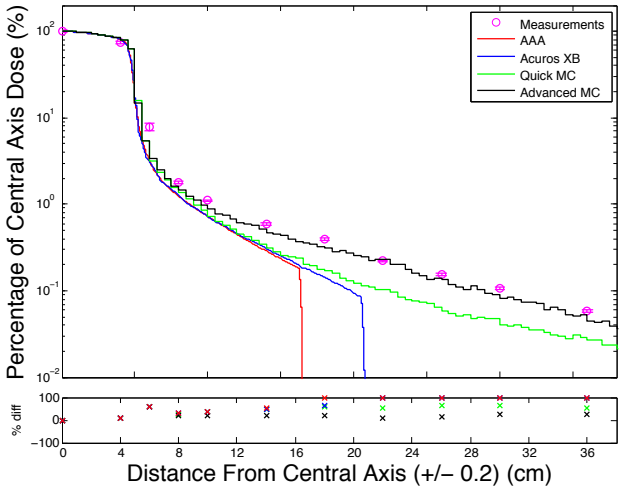

(a) 10X-FFF, depth of 5 cm

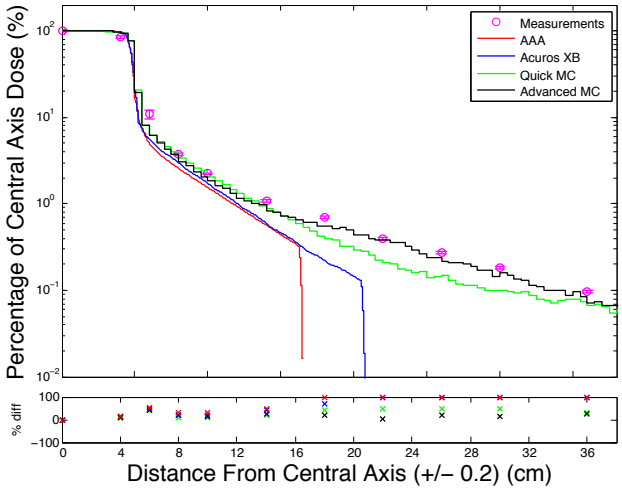

(b) 6X, depth of 5 cm

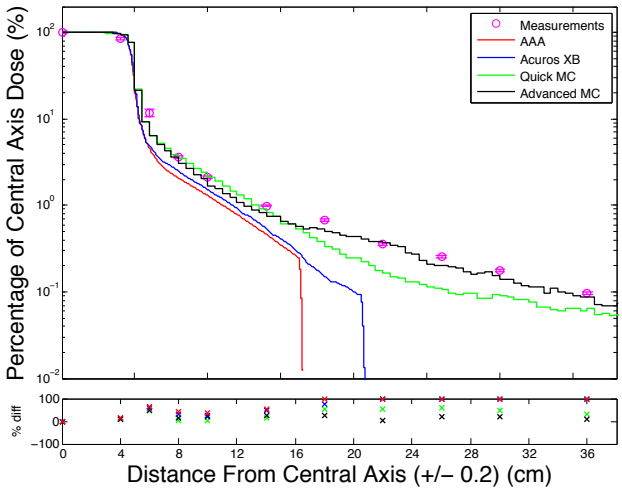

(c) 10X, depth of 5 cm

Figure A.3: Static open field dose calculation algorithm comparison for three energies.

Appendix B

Additional Information

Additional figures and tables from chapter 5 are found in this appendix.

B.1 Monte Carlo Simulations - Static Gantry Delivery

The VMAT lung SABR plans using 10XFFF, 6X and 10X for each of the six cases were calculated in the solid water phantom.

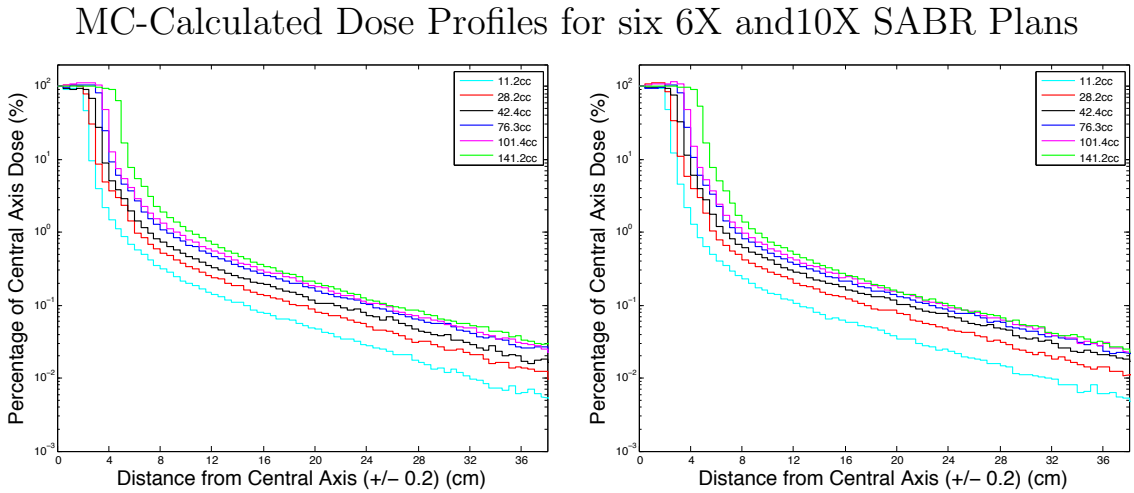

(a) 6X (b) 10X

Figure B.1: Relative dose at a depth of 10 cm as a function of distance from the CAX in the Superior-Inferior direction, for six cases, according to PTV volume.

Superior-Inferior profiles were taken for each plans at depths of 10 cm and 5 cm.

The profiles for the six plans using 10X-FFF are shown at a depth of 10 cm in chapter 5, figure 5.1.

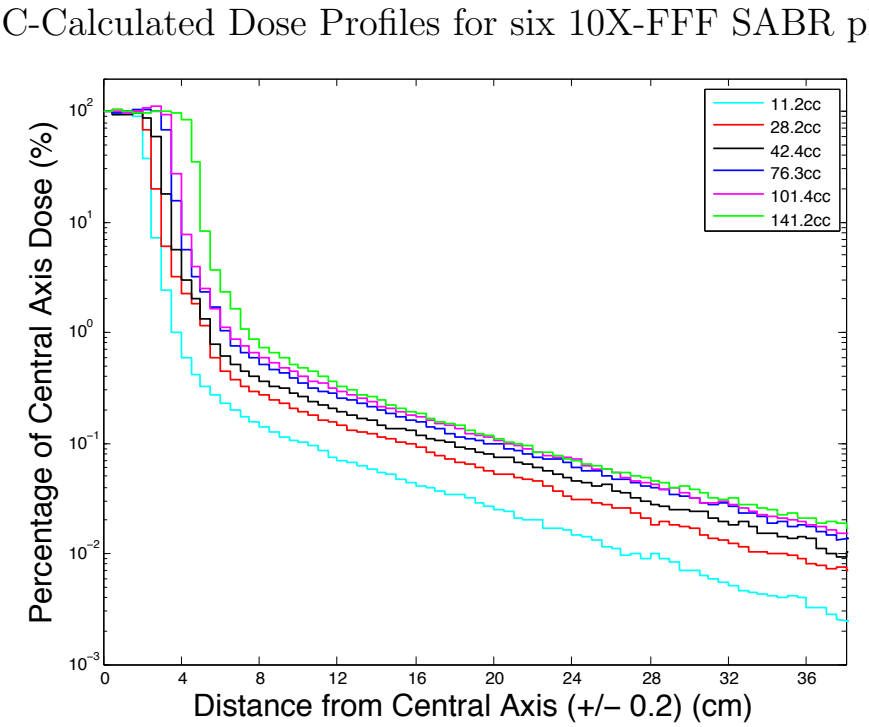

Figure B.2: Relative dose at a depth of 5 cm as a function of distance from the CAX in the Superior-Inferior direction, for six cases, according to PTV volume.

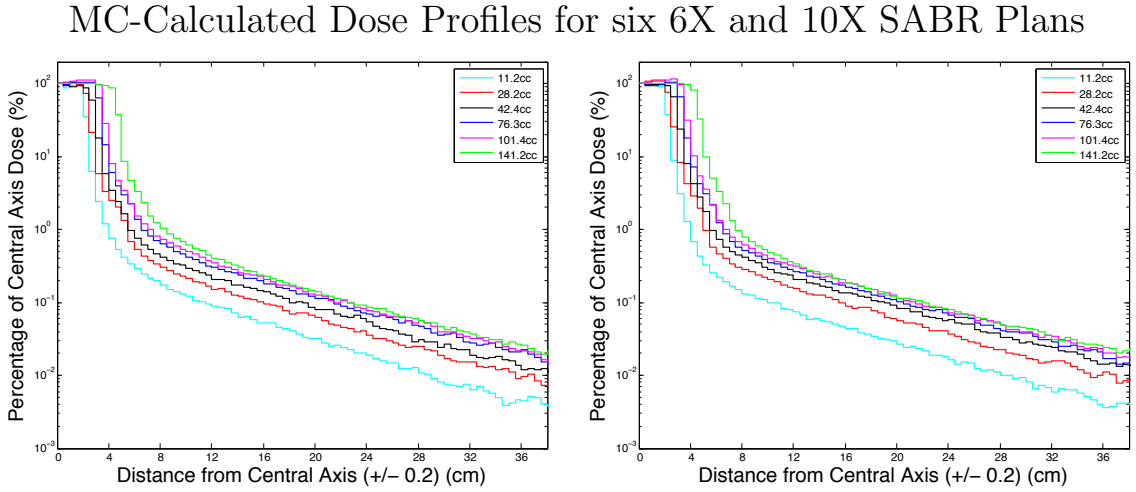

(a) 6X (b) 10X

Figure B.3: Relative dose at a depth of 5 cm as a function of distance from the CAX in the Superior-Inferior direction, for six cases, according to PTV volume.

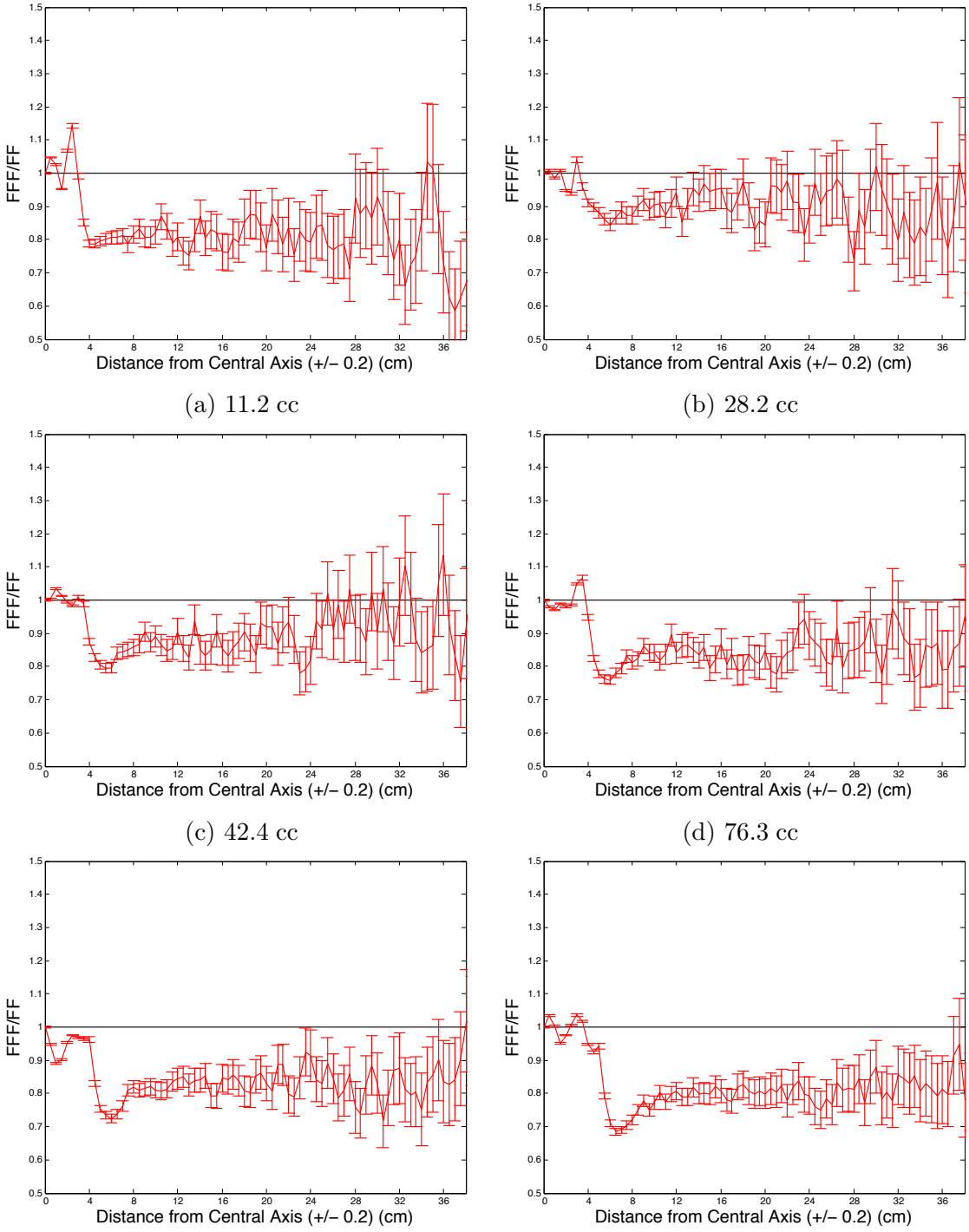

(a) 11.2 cc

(b) 28.2 cc

(c) 42.4 cc

(d) 76.3 cc

(e) 101.4 cc

(f) 141.2 cc

Figure B.4: FFF/FF ratio for 10X-FFF compared to 6X plans, at a depth of 5 cm in the solid water phantom, for each of the six cases.

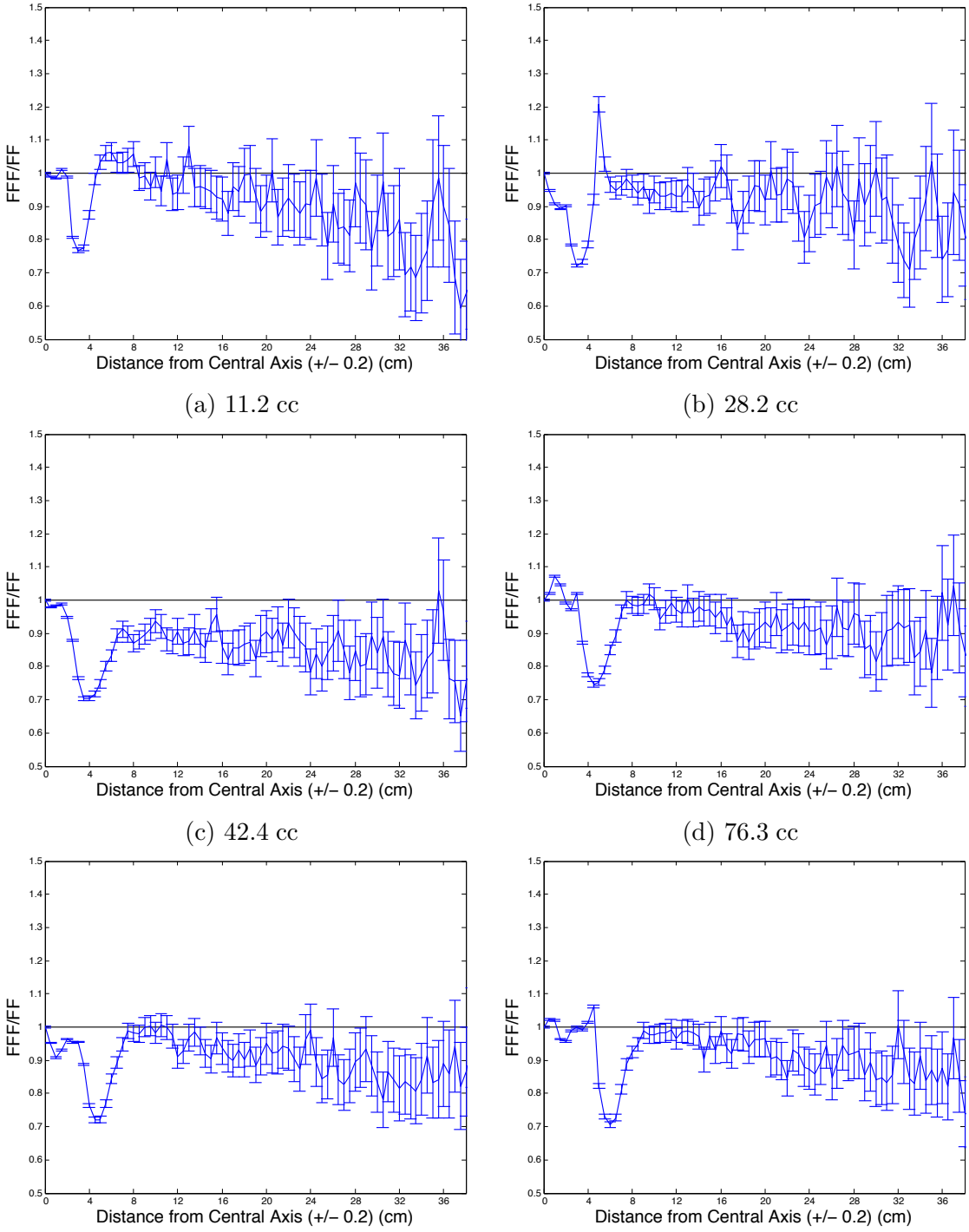

(a) 11.2 cc

(b) 28.2 cc

(c) 42.4 cc

(d) 76.3 cc

(e) 101.4 cc

(f) 141.2 cc

Figure B.5: FFF/FF ratio for 10X-FFF compared to 10X plans, at a depth of 5 cm in the solid water phantom, for each of the six cases.

Bibliography

[1] E. B. Podgorsak, *Radiation Physics for Medical Physicists*. Springer-Verlag Berlin Heidelberg, 2006.

[2] F. M. Khan, *The Physics of Radiation Therapy - 3rd edition*. Lippincott Williams & Wilkins, 2003.

[3] M. Joiner and A. van der Kogel, *Basic Clinical Radiobiology , 4th edition*. Hodder Arnold, 2009.

[4] G. Delaney, S. Jacob, C. Featherstone, and M. Barton, "The role of radiotherapy in cancer treatment: estimating optimal utilization from a review of evidence-based clinical guidelines.," *Cancer*, vol. 104, pp. 1129–1137, Sept. 2005.

[5] Canadian Partnership Against Cancer, *The 2012 Cancer System Performance Report*. Canadian Partnership Against Cancer, 2012.

[6] Statistics Canada, "Table 103-0553 - New cases and age-standardized rate for primary cancer (based on the February 2014 CCR tabulation file), by cancer type and sex, Canada, provinces and territories, annual, CANSIM (database)." Accessed: 2014-10-24.

[7] S. H. Levitt, J. A. Purdy, C. A. Perez, and S. Vijayakumar, *Technical Basis of Radiation Therapy - Practical Clinical Applications, 4th ed.* Springer-Verlag Berlin Heidelberg, 2006.

[8] K. Otto, "Volumetric modulated arc therapy: IMRT in a single gantry arc.," *Medical Physics*, vol. 35, no. 1, pp. 310–317, 2008.

[9] C. R. Lund, "Protocol Guidelines for Stereotactic Body Radiotherapy (SBRT) for Primary Early Stage NSCLC in British Columbia.," July 2011.

[10] J. Hrbacek, S. Lang, S. N. Graydon, S. Klöck, and O. Riesterer, "Dosimetric comparison of flattened and unflattened beams for stereotactic ablative radiotherapy of stage I non-small cell lung cancer.," *Medical Physics*, vol. 41, pp. 1–7, Mar. 2014.

[11] S. F. Kry, O. N. Vassiliev, and R. Mohan, "Out-of-field photon dose following removal of the flattening filter from a medical accelerator.," *Physics in Medicine and Biology*, vol. 55, pp. 2155–2166, Apr. 2010.

[12] P. F. O'Brien, "Radiosurgery with unflattened 6-MV photon beams.," *Medical Physics*, vol. 18, no. 3, pp. 519–521, 1991.

[13] D. Georg, T. Knöös, and B. McClean, "Current status and future perspective of flattening filter free photon beams.," *Medical Physics*, vol. 38, no. 3, pp. 1280–1293, 2011.

[14] I. Diallo, N. Haddy, E. Adjadj, A. Samand, E. Quiniou, J. Chavaudra, I. Alziar, N. Perret, S. Guérin, D. Lefkopoulos, and F. de Vathaire, "Frequency distribution of second solid cancer locations in relation to the irradiated volume among 115 patients treated for childhood cancer.," *International Journal of Radiation Oncology, Biology, Physics*, vol. 74, pp. 876–83, July 2009.

[15] X. G. Xu, B. Bednarz, and H. Paganetti, "A review of dosimetry studies on external-beam radiation treatment with respect to second cancer induction.," *Physics in Medicine and Biology*, vol. 53, pp. R193–R241, June 2008.

[16] S. F. Kry, M. Salehpour, D. S. Followill, M. Stovall, D. Kuban, R. A. White, and I. I. Rosen, "The calculated risk of fatal secondary malignancies from intensity-modulated radiation therapy.," *International Journal of Radiation Oncology, Biology, Physics*, vol. 62, pp. 1195–1203, July 2005.

[17] C. L. Ong, W. Verbakel, M. Dahele, J. P. Cuijpers, B. J. Slotman, and S. Senan, "Fast arc delivery for stereotactic body radiotherapy of vertebral and lung tumors.," *International Journal of Radiation Oncology, Biology, Physics*, vol. 83, pp. e137–e143, May 2012.

[18] P. Mancosu, S. Castiglioni, G. Reggiori, M. Catalano, F. Alongi, C. Pellegrini, S. Arcangeli, A. Tozzi, F. Lobefalo, A. Fogliata, P. Navarria, L. Cozzi, and

M. Scorsetti, "Stereotactic body radiation therapy for liver tumours using flattening filter free beam: dosimetric and technical considerations.," *Radiation Oncology*, vol. 7, pp. 16–23, Jan. 2012.

[19] G. Nicolini, S. Ghosh-Laskar, S. K. Shrivastava, S. Banerjee, S. Chaudhary, P. Agarwal, A. Munshi, A. Clivio, A. Fogliata, P. Mancosu, E. Vanetti, and L. Cozzi, "Volumetric modulation arc radiotherapy with flattening filter-free beams compared with static gantry IMRT and 3D conformal radiotherapy for advanced esophageal cancer : a feasibility study.," *Radiation Oncology Biology*, vol. 84, no. 2, pp. 553–560, 2012.

[20] M. Scorsetti, F. Alongi, S. Castiglioni, A. Clivio, A. Fogliata, F. Lobefalo, P. Mancosu, P. Navarria, V. Palumbo, C. Pellegrini, S. Pentimalli, G. Reggiori, A. M. Ascolese, A. Roggio, S. Arcangeli, A. Tozzi, E. Vanetti, and L. Cozzi, "Feasibility and early clinical assessment of flattening filter free (FFF) based stereotactic body radiotherapy (SBRT) treatments.," *Radiation Oncology*, vol. 6, pp. 113–120, Jan. 2011.

[21] G. Kragl, F. Baier, S. Lutz, D. Albrich, M. Dalaryd, B. Kroupa, T. Wiezorek, T. Knöös, and D. Georg, "Flattening filter free beams in SBRT and IMRT: dosimetric assessment of peripheral doses.," *Zeitschrift fur Medizinische Physik*, vol. 21, pp. 91–101, May 2011.

[22] C. J. Karzmark, C. S. Nunan, and E. Tanabe, *Medical Electron Accelerators*. McGraw-Hill, Inc. Health Professions Division, 1993.

[23] F. H. Attix, *Introduction to Radiological Physics and Radiation Dosimetry*. Wiley-Interscience, 1986.

[24] H. C. John and J. R. Cunningham, *The Physics of Radiology, 4th ed.* Charles C. Thomas, 1983.

[25] M. L. Taylor, L. N. McDermott, P. N. Johnston, M. Haynes, T. Ackerly, T. Kron, and R. D. Franich, "Stereotactic fields shaped with a micro-multileaf collimator: systematic characterization of peripheral dose.," *Physics in Medicine and Biology*, vol. 55, pp. 873–881, Feb. 2010.

[26] E. J. Hall, *Radiobiology for the Radiologist - 5th ed.* Lippincott Williams & Wilkins, 2000.

[27] M. Stovall, C. R. Blackwell, J. Cundiff, D. H. Novack, J. R. Palta, L. K. Wagner, and R. J. Shalek, "Fetal Dose from Radiotherapy with photon beam: Report of AAPM Radiation Therapy Committee Task Group No. 36.," *Medical Physics*, vol. 22, no. 1, pp. 63–82, 1995.

[28] M. Stovall, C. R. Blackwell, J. Cundiff, D. H. Novack, J. R. Palta, L. K. Wagner, and R. J. Shalek, "Erratum: "Fetal Dose from Radiotherapy with photon beam: Report of AAPM Radiation Therapy Committee Task Group No. 36" (Med. Phys. 22, 63-82 (1995))," *Medical Physics*, vol. 22, no. 8, pp. 1353–1354, 1995.

[29] E. J. Hall and C.-S. Wuu, "Radiation-induced second cancers: the impact of 3D-CRT and IMRT.," *International Journal of Radiation Oncology, Biology, Physics*, vol. 56, pp. 83–88, May 2003.

[30] E. J. Hall and D. Phil, "Intensity-Modulated Radiation Therapy, protons, and the risk of second cancers.," *International Journal of Radiation Oncology, Biology, Physics*, vol. 65, no. 1, pp. 1–7, 2006.

[31] M. J. Butson, T. Cheung, and P. K. N. Yu, "XR type-R radiochromic film x-ray energy response.," *Physics in Medicine and Biology*, vol. 50, pp. N195–N199, Aug. 2005.

[32] O. N. Vassiliev, U. Titt, F. Pönisch, S. F. Kry, R. Mohan, and M. T. Gillin, "Dosimetric properties of photon beams from a flattening filter free clinical accelerator.," *Physics in Medicine and Biology*, vol. 51, pp. 1907–1917, Apr. 2006.

[33] M. Dalaryd, G. Kragl, C. Ceberg, D. Georg, B. McClean, S. Wetterstedt, E. Wieslander, and T. Knöös, "A Monte Carlo study of a flattening filter-free linear accelerator verified with measurements.," *Physics in Medicine and Biology*, vol. 55, pp. 7333–7344, Dec. 2010.

[34] G. Kragl, S. Wetterstedt, B. Knäusl, M. Lind, P. McCavana, T. Knöös, B. McClean, and D. Georg, "Dosimetric characteristics of 6 and 10MV unflattened photon beams.," *Radiotherapy and Oncology : Journal of the European Society for Therapeutic Radiology and Oncology*, vol. 93, pp. 141–146, Oct. 2009.

[35] J. Cashmore, M. Ramtohul, and D. Ford, "Lowering whole-body radiation doses in pediatric intensity-modulated radiotherapy through the use of unflattened

photon beams.," *International Journal of Radiation Oncology, Biology, Physics*, vol. 80, pp. 1220–1227, July 2011.

[36] Varian Medical Systems, *Eclipse Algorithms Reference Guide*. Varian Medical Systems, Palo Alto, CA, Dec. 2013.

[37] R. M. Howell, S. B. Scarboro, S. F. Kry, and D. Z. Yaldo, "Accuracy of out-of-field dose calculations by a commercial treatment planning system.," *Physics in Medicine and Biology*, vol. 55, pp. 6999–7008, Dec. 2010.

[38] T. Han, D. Followill, J. Mikell, R. Repchak, A. Molineu, R. Howell, M. Salehpour, and F. Mourtada, "Dosimetric impact of Acuros XB deterministic radiation transport algorithm for heterogeneous dose calculation in lung cancer.," *Medical Physics*, vol. 40, no. 5, p. 051710, 2013.

[39] G. Cowan, *Statistical Data Analysis*. Oxford University Press, 1998.

[40] I. J. Chetty, B. Curran, J. E. Cygler, J. J. DeMarco, G. Ezzell, B. Faddegon, I. Kawrakow, P. J. Keall, H. Liu, C. C.-M. Ma, D. W. O. Rogers, J. Seuntjens, D. Sheikh-Bagheri, and J. V. Siebers, "Report of the AAPM Task Group No. 105: Issues associated with clinical implementation of Monte Carlo-based photon and electron external beam treatment planning.," *Medical Physics*, vol. 34, no. 12, pp. 4818–4853, 2007.

[41] I. Kawrakow, E. Mainegra-Hing, D. W. O. Rogers, F. Tessier, and B. R. B. Walters, *The EGSnrc Code System: Monte Carlo Simulation of Electron and Photon Transport.* NRC Canada, 2001-2011.

[42] D. W. O. Rogers, B. Walters, and I. Kawrakow, *BEAMnrc Users Manual.* NRC Canada, 2007.

[43] B. Walters, I. Kawrakow, and D. W. O. Rogers, *DOSXYZnrc Users Manual.* NRC Canada, 2011.

[44] J. V. Siebers, P. J. Keall, J. O. Kim, and R. Mohan, "A method for photon beam Monte Carlo multileaf collimator particle transport.," *Physics in Medicine and Biology*, vol. 47, pp. 3225–3249, Sept. 2002.

[45] J. Gardner, J. Siebers, and J. Kawrakow, "Dose calculation validation of VMC++ for photon beams.," *Medical Physics*, vol. 34, no. 5, pp. 1809–1818, 2007.

[46] P. R. Almond, P. J. Biggs, B. M. Coursey, W. F. Hanson, M. S. Huq, R. Nath, and D. W. Rogers, "AAPM's TG-51 protocol for clinical reference dosimetry of high-energy photon and electron beams.," *Medical Physics*, vol. 26, pp. 1847–1870, Sept. 1999.

[47] S. F. Kry, R. Popple, A. Molineu, and D. S. Followill, "Ion recombination correction factors (P_{ion}) for Varian TrueBeam high-dose-rate therapy beams.," *Journal of Applied Clinical Medical Physics / American College of Medical Physics*, vol. 13, pp. 318–325, Jan. 2012.

[48] B. Walters, I. Kawrakow, and D. W. O. Rogers, "History by history statistical estimators in the BEAM code system.," *Medical Physics*, vol. 29, no. 12, pp. 2745–2752, 2002.

[49] S. S. Almberg, J. Frengen, and T. Lindmo, "Monte Carlo study of in-field and out-of-field dose distributions from a linear accelerator operating with and without a flattening-filter.," *Medical Physics*, vol. 39, no. 8, pp. 5194–5203, 2012.

[50] K. H. Spruijt, M. Dahele, J. P. Cuijpers, M. Jeulink, D. Rietveld, B. J. Slotman, and W. Verbakel, "Flattening filter free vs flattened beams for breast irradiation.," *International Journal of Radiation Oncology, Biology, Physics*, vol. 85, pp. 506–513, Feb. 2013.

[51] T. Kairn, S. B. Crowe, and J. V. Trapp, "Correcting radiation survey data to account for increased leakage during intensity modulated radiotherapy treatments.," *Medical Physics*, vol. 40, p. 111708, Nov. 2013.

[52] International Commission on Radiological Protection, "ICRP Publication 103: Recommendations of the ICRP.," *Radiation Protection Dosimetry*, vol. 129, no. 4, pp. 500–507, 2008.